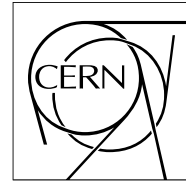


The Compact Muon Solenoid Experiment

# Analysis Note

The content of this note is intended for CMS internal use and distribution only



09 January 2013 (v7, 10 December 2013)

## Search for quark contact interactions and extra spatial dimensions in the dijet angular distributions at 8 TeV

Leonard Apanasevich (University of Illinois at Chicago), Suvadeep Bose (University of Nebraska Lincoln), Inga Bucinskaite (University of Illinois at Chicago), Andreas Hinzmann (University of Zurich), Klaus Rabbertz (Karlsruhe Institute of Technology), Nikos Varelas (University of Illinois at Chicago)

### Abstract

Measurements of the dijet angular distributions using 8 TeV pp collision data taken by the CMS experiment and corresponding to an integrated luminosity of 19.7/fb are presented. Excellent agreement with NLO QCD predictions is found. The scattering angle distribution of quark-quark interactions as predicted by QCD may be modified by additional contact interactions which arise in quark compositeness models as well as virtual graviton exchange which arises in the ADD large extra dimension model. We set limits on various possible contact interactions. The benchmark scenario where only left-handed quarks participate evaluated up to NLO in QCD is excluded up to a scale of 8.8 TeV. We set limits on the ADD model according to GRW and HLZ conventions. In the GRW convention, virtual graviton exchange is excluded up to a scale of 7.0 TeV.

This box is only visible in draft mode. Please make sure the values below make sense.

PDFAuthor:	Leonard Apanasevich, Suvadeep Bose, Inga Bucinskaite, Andreas Hinzmann, Klaus Rabbertz, Nikos Varelas
PDFTitle:	Searches for quark contact interactions and extra spatial dimensions with dijet angular distributions in proton proton collisions at 8 TeV
PDFSubject:	CMS
PDFKeywords:	CMS, physics, QCD, contact interactions, extra dimensions

Please also verify that the abstract does not use any user defined symbols

DRAFT

# 1 Introduction

High energy proton-proton collisions with large momentum transfers predominantly produce events containing two jets (dijets) with high transverse momenta ( $p_T$ ). Such events probe the interacting partons at the shortest distance scales and provide a fundamental test of quantum chromodynamics (QCD). They can also be used to test the standard model (SM) at previously unexplored small distance scales, to search for signals predicted by new physics models, such as substructure of quarks (quark compositeness), and additional compactified spatial dimensions.

The dijet angular distribution probes the properties of parton-parton scattering without strong dependence on the parton distribution functions (PDFs). The reason for this is the dominance of the t-channel gluon exchange in the three main scattering processes,  $qg \rightarrow qg$ ,  $q\bar{q}(q') \rightarrow q\bar{q}(q')$ , and  $gg \rightarrow gg$ , which makes their angular distributions similar. The dijet angular distribution is typically expressed in terms of  $\chi_{dijet} = \exp(|y_1 - y_2|)$ , where  $y_1$  and  $y_2$  are the rapidities of the two leading jets,  $y \equiv \frac{1}{2} \ln [(E + p_z) / (E - p_z)]$ , and  $p_z$  is the projection of the jet momentum on the beam axis. The choice of this variable was motivated by the fact that Rutherford scattering the  $\chi_{dijet}$  distribution is flat. It also allows signatures of new physics that might have a more isotropic angular distribution than QCD (e.g., quark compositeness) to be more easily examined as they would produce an excess at low values of  $\chi_{dijet}$ . Measurements of dijet angular distributions have previously been reported at the Tevatron by the D0 [1, 2] and CDF [3] collaborations, and at the LHC by the ATLAS [4–6] and CMS [7–9] collaborations.

A common signature of quark compositeness models is the appearance of new interactions between quark constituents at a characteristic scale  $\Lambda$  that is much larger than the quark masses. At energies well below  $\Lambda$ , these interactions can be approximated by a contact interaction (CI) [10, 11] characterized by a four-fermion coupling. In this letter, flavor-diagonal color-singlet couplings between quarks are studied. These can be described by the effective Lagrangian [10, 12]

$$L_{qq} = \frac{2\pi}{\Lambda^2} [\eta_{LL}(\bar{q}_L \gamma^\mu q_L)(\bar{q}_L \gamma_\mu q_L) + \eta_{RR}(\bar{q}_R \gamma^\mu q_R)(\bar{q}_R \gamma_\mu q_R) + 2\eta_{RL}(\bar{q}_R \gamma^\mu q_R)(\bar{q}_L \gamma_\mu q_L)],$$

where the subscripts  $L$  and  $R$  refer to the chiral projections of the quark fields and  $\eta_{LL}$ ,  $\eta_{RR}$ , and  $\eta_{RL}$  can be 0, +1, or −1. The various combinations of  $\eta_{LL}$ ,  $\eta_{RR}$ , and  $\eta_{RL}$  correspond to different CI models. The following CI scenarios are investigated:

$$\begin{aligned} \Lambda &= \Lambda_{LL}^\pm \text{ for } (\eta_{LL}, \eta_{RR}, \eta_{RL}) = (\pm 1, 0, 0), \\ \Lambda &= \Lambda_{RR}^\pm \text{ for } (\eta_{LL}, \eta_{RR}, \eta_{RL}) = (0, \pm 1, 0), \\ \Lambda &= \Lambda_{VV}^\pm \text{ for } (\eta_{LL}, \eta_{RR}, \eta_{RL}) = (\pm 1, \pm 1, \pm 1), \\ \Lambda &= \Lambda_{AA}^\pm \text{ for } (\eta_{LL}, \eta_{RR}, \eta_{RL}) = (\pm 1, \pm 1, \mp 1), \\ \Lambda &= \Lambda_{(V-A)}^\pm \text{ for } (\eta_{LL}, \eta_{RR}, \eta_{RL}) = (0, 0, \pm 1). \end{aligned}$$

In pp collisions these models result in the same limits for  $\Lambda_{LL}^\pm$  and  $\Lambda_{RR}^\pm$ , and at tree level for  $\Lambda_{VV}^\pm$  and  $\Lambda_{AA}^\pm$  as well as for  $\Lambda_{(V-A)}^+$  and  $\Lambda_{(V-A)}^-$ . The most stringent limits on these models come from the searches studying the dijet angular distributions [7] at high jet-jet masses and inclusive jet  $p_T$  [13] distribution.

The dijet angular distributions are also sensitive to signatures from extra dimension models. The existence of compactified extra dimensions as proposed in the Arkani-Hamed-Dimopoulos-Dvali (ADD) model [14, 15] provides a possible solution to the hierarchy problem of the SM. In the ADD model, gravity is assumed to propagate in the entire higher-dimensional space, while SM particles are confined to a 3+1 dimensional subspace. As a result, the fundamental Planck scale  $M_D$  in the ADD model is much smaller than the 3+1 dimensional Planck energy scale  $M_{Pl}$ , which may lead to phenomenological effects that can be tested with proton-proton collisions at the LHC. The coupling of the Kaluza-Klein modes to the SM energy-momentum tensor can be approximated by an effective theory with virtual graviton exchange at leading order in perturbation theory. Such a theory predicts a non-resonant enhancement of dijet production, whose angular distribution differs from QCD prediction. We consider two parametrizations for virtual graviton exchange in the ADD model, namely the GRW (Giudice, Rattazzi, Wells) [16] and the HLZ (Han, Lykken, Zhang) [17] convention. In the GRW convention, the phenomenology after summing over the Kaluza-Klein states is controlled by a single parameter  $\Lambda_T$ . The HLZ convention describes the phenomenology in terms of the parameters  $M_S$  and  $n_{ED}$ , where  $M_S$  represents a string scale expected to be of order  $M_D$  and  $n_{ED}$  is the number of extra dimensions in a  $4+n_{ED}$  dimensional space. The parameters  $M_S$  and  $n_{ED}$  can be directly related to  $\Lambda_T$  [?]. We consider scenarios with 2 to 6 extra dimensions. The case of  $n_{ED} = 1$  is not considered since it would require extra dimensions of sizes larger than 1 mm, which are already excluded experimentally. The case of  $n_{ED} = 2$  is special in the sense that the relation between  $M_S$  and  $\Lambda_T$  also depends on the parton-parton center of mass energy  $\sqrt{\hat{s}}$ . The effective theory is expected to break down at an energy scale of order  $M_D$ . Therefore the range of  $M_S$  which we explore is higher than the highest dijet mass we measure. Signatures from virtual graviton exchange have previously been searched for in dilepton [18, 19], diphoton [20, 21] and dijet [22, 23] final states where the most stringent limits come from the dijet search [23].

In this paper, our previous searches are extended to higher contact interaction (CI) scales using a data sample corresponding to an integrated luminosity of  $19.7 \text{ fb}^{-1}$  at  $\sqrt{s} = 8 \text{ TeV}$ , exploring a wide range of CI and extra dimension models. We first present the measurement of the dijet angular distributions unfolded for detector effects and then search for evidence for CI and extra dimension signatures.

The Compact Muon Solenoid (CMS) detector is described in detail elsewhere [24]. In this study, jets are identified using energy depositions from the lead-tungstate crystal electromagnetic calorimeter (ECAL) and the brass-scintillator hadronic calorimeter (HCAL). These calorimeters provide a uniform and hermitic coverage over a large range of pseudorapidity ( $|\eta| \leq 5$ , where  $\eta \equiv -\ln \tan(\theta/2)$  and  $\theta$  is the polar angle relative to the proton beam.) The calorimeter cells are grouped in projective towers of granularity  $\Delta\eta \times \Delta\phi = 0.087 \times 0.087$  ( $0.175 \times 0.175$ ) at central (forward) rapidities. CMS uses a right-handed coordinate system, with the origin located at the nominal collision point, the  $x$ -axis pointing towards the center of the LHC, the  $y$ -axis pointing up (perpendicular to the LHC plane), and the  $z$ -axis along the (anticlockwise) beam direction.

This analysis note is structured as follows. In Section 2 the observables and analysis phase space are defined. Section 3 summarizes the jet reconstruction and identification. Data samples, triggers, event selection, data-MC comparisons, the unfolding correction applied to the data and the systematic uncertainties are presented in Section 4. The theory prediction is discussed in Section 5. The final result, the comparison of the unfolded data to the theory prediction, is shown in Section 6. Section 7 describes the limit setting procedure on a contact interaction model using the angular distributions.

## 2 Definition of Observable and Phase Space

The dijet system consists of the two largest transverse momentum jets in the event. The dijet mass is formally expressed as:

$$M_{jj}^2 = P_{j_1}^\mu P_{\mu, j_2} = (E_1 + E_2)^2 - (\vec{p}_1 + \vec{p}_2)^2 \quad (1)$$

where  $P_{ji}^\mu = (E_i, \vec{p}_i)$  are the four-momenta of the two leading jets. In the limit of massless jets, the dijet mass can be expressed in terms of measured jet quantities as

$$M_{jj}^2 = 2p_{T_1} p_{T_2} [\cosh(\eta_1 - \eta_2) - \cos(\phi_1 - \phi_2)]. \quad (2)$$

As mentioned in the Introduction, the angular distribution is characterized by  $\chi_{dijet} = \exp(2y^*)$  where  $y^* = \frac{1}{2}|y_1 - y_2|$ . In massless  $2 \rightarrow 2$  scattering processes,  $\pm y^*$  are the rapidities of the two jets in the dijet center-of-mass frame which are related to the scattering angle in this frame,  $\theta^*$ , by  $y^* = \frac{1}{2} \ln \left( \frac{1 + |\cos \theta^*|}{1 - |\cos \theta^*|} \right)$ . In this approximation the dijet angular variable  $\chi_{dijet}$  can be written as  $\chi_{dijet} = \frac{1 + |\cos \theta^*|}{1 - |\cos \theta^*|}$ . The variable  $y_{boost} = \frac{1}{2}(y_1 + y_2)$  denotes the average rapidity of the two jets. In massless  $2 \rightarrow 2$  scattering processes,  $y_{boost}$  specifies the longitudinal boost by which the dijet center-of-mass frame is boosted with respect to the detector frame.

### 2.1 Definition of Phase Space

In this analysis, the  $\chi_{dijet}$  distribution is measured over the range  $1 < \chi_{dijet} < 16$ , which implies a maximum value of  $y^* = 1.39$ . The rapidity of each jet is restricted to  $|y| = 2.5$  so that the jets were contained in a well understood region of the calorimeter. The maximum value of  $y_{boost}$  is constrained to  $|y_{boost}| < 1.11$ , since the variables  $y_{boost}$ ,  $y^*$ , and  $y_{max}$  satisfy the inequality:  $|y_{boost}| + y^* < |y_{max}|$ .

The dijet angular distributions are measured in 5 bins of dijet mass: 1.9-2.4, 2.4-3.0, 3.0-3.6, 3.6-4.2, 4.2- $\infty$  TeV. The minimum mass threshold is chosen above the point where the jet triggers are fully efficient. The remaining dijet mass bins are chosen with a width well above the dijet mass resolution, requiring at least 20 events in highest mass bin, to allow a measurement of the shape of the angular distribution.

## 3 Jet Reconstruction

Particle flow jets were used to study the angular distribution of dijets. These jets are reconstructed using particles (charged hadron, neutral hadrons, electrons, muons and photons) reconstructed using all detector components (tracker, calorimeters and muon system) as input, excluding charged particles which do not originate from the primary vertex in the event. Jets are formed using the anti-kT clustering algorithm with cone size  $R = \sqrt{(\Delta\eta^2) + (\Delta\phi^2)} = 0.5$ . To compare the data with NLO and PYTHIA predictions, particle-level jets are made by applying the same jet clustering algorithm to the Lorentz vectors of stable particles generated in the case of PYTHIA, and to the outgoing partons in the case of NLO predictions.

### 3.1 Jet Identification

A set of jet identification (JetID) requirements has been determined to remove jets created from unphysical energy depositions in the calorimeter (e.g. noise, hot cells) [25]. For this analysis,

the “tight” JetID selection criteria for particle flow jets have been applied. These criteria include requirements on the neutral hadron fraction (NHF), neutral electromagnetic fraction (NEF), charged hadron fraction (CHF), charged electromagnetic fraction (CEF), number of constituents ( $n_{\text{constituents}}$ ) and charged multiplicity ( $n_{\text{charged}}$ ). These requirements are summarized in Table 1. In addition, jets with a muon energy fraction greater than 0.8 are rejected to suppress noise from misreconstructed high energy muons. For jets with  $p_T$  greater than 30 GeV, losses due to the application of these selection criteria are estimated to be less than 1%.

Table 1: Tight particle flow jet quality criteria

variable	$ \eta $	tight JetID
$NHF$		$< 0.9$
$NEF$		$< 0.9$
$CHF$	$< 2.4$	$> 0$
$CEF$	$< 2.4$	$< 0.99$
$n_{\text{constituents}}$		$> 1$
$n_{\text{charged}}$	$< 2.4$	$> 0$

### 3.2 Jet Energy Scale Corrections

The transverse momenta of jets were corrected for the response of the detector using the relative ( $\eta$ ) and absolute ( $p_T$ ) jet corrections developed by the JetMET POG [26] in GlobalTags START53\_V23 and FT\_53\_V21\_AN4. These corrections are a combination of MC truth corrections determined from QCD events generated by PYTHIA [27] and were further processed using a full, GEANT4-based [28] detector simulation and a residual correction determined from the absolute and relative jet response measured in dijet and photon+jet data. The corresponding uncertainties are parametrized as a function of  $\eta$  and  $p_T$  and range from 2%-3% for particle flow jets with  $p_T > 30$  GeV.

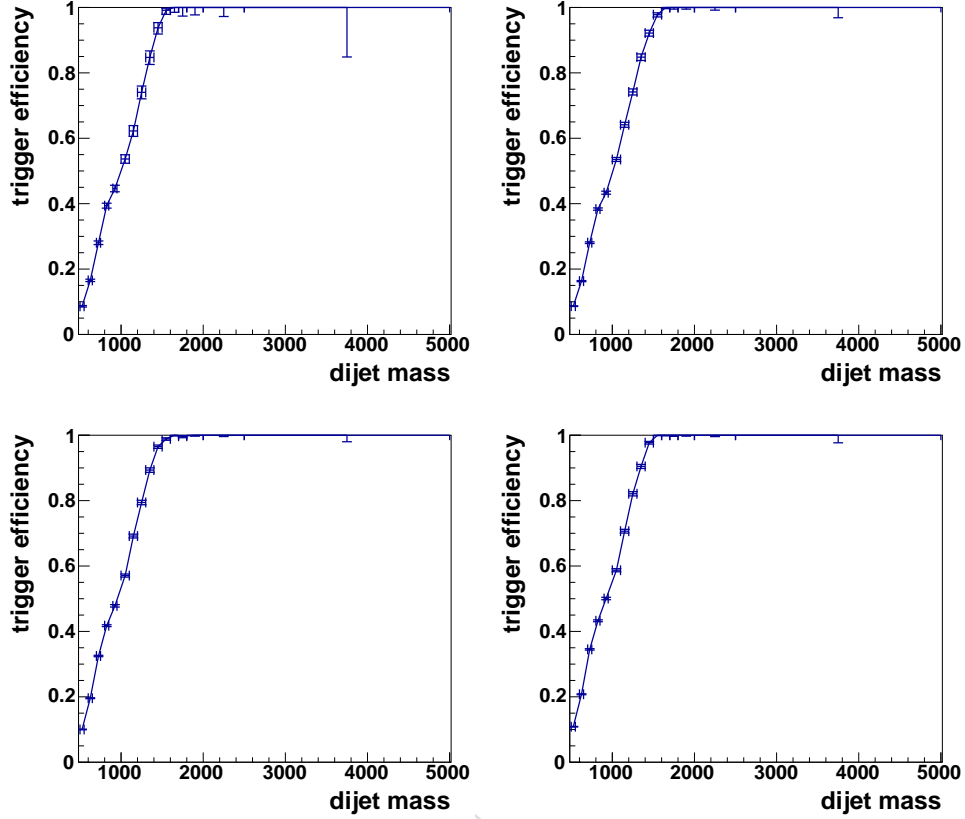


Figure 1: Trigger efficiency in Run2012A (top left), B (top right), C (bottom left) and D (bottom right) as a function of dijet mass.

## 4 Data Analysis

The data presented in this analysis corresponds to  $19.7 \text{ fb}^{-1}$  of integrated luminosity collected in 2012. The analysis was done using officially validated input events from the following datasets:

```
/HT/Run2012A-Jan22ReReco-v1/AOD
/JetHT/Run2012B-Jan22ReReco-v1/AOD
/JetHT/Run2012C-Jan22ReReco-v1/AOD
/JetHT/Run2012D-Jan22ReReco-v1/AOD
```

The selection of good runs and luminosity sections was technically implemented by using officially produced JSON files.

### 4.1 Triggers

The CMS trigger uses a two-tiered system to select physics events of interest for further analysis; Level-1 Trigger (L1) and High-Level Trigger (HLT). The trigger paths used in this analysis were the inclusive single jet triggers which required a Level-1 jet and an HLT jet with certain thresholds of scalar sums of transverse momentum or dijet mass requirements (HT750 — PF-Jet400 — DiPFJetAve400 — PFHT650 — FatDiPFJetMass750). The trigger paths use jets that are corrected for the response of the calorimeter at both Level-1 and HLT.

The efficiencies have been measured using a lower threshold reference trigger (HT450) within

our analysis phase space as defined in Section 2. The efficiency was partly measured in runs with prescaled reference triggers. Therefore the turn-on curves were scaled by the effective luminosities of the triggers. The first mass bin in Table 2 was chosen well above the 99% efficiency point for the corresponding trigger.

## 4.2 Event Selection

Beam scraping events were filtered away by cutting on the fraction of high-purity tracks with respect to the total number of tracks, required to be at least 25% when the event has at least 10 tracks. A primary vertex is required to be reconstructed from at least 5 tracks (fit  $n_{\text{dof}} > 4$ ) with  $|z_{\text{PV}}| < 24$  cm with  $\rho_{\text{PV}} = \sqrt{x_{\text{PV}}^2 + y_{\text{PV}}^2} < 2$  cm. Filters for HCAL laser events, tracking failure, HBHE noise, ECAL dead cell trigger primitive, CSC tight halo are applied. Finally events with the first two jets passing the tight jet ID and muon fraction smaller than 0.8 (as described in Section 3.1) are selected and the analysis phase space cuts are applied. The final number of data events in each mass bin is summarized in Table 2

Table 2: The final number of data events in each mass bins. Efficiencies obtained from Madgraph+Pythia6 QCD MC are given in brackets.

Mass bin [TeV]	# events
1.9-2.4	147707
2.4-3.0	24048
3.0-3.6	3023
3.6-4.2	364
4.2- $\infty$	50

## 4.3 Comparisons with the Detector Simulation

A detailed simulation of the CMS spectrometer has been developed using the GEANT4 package to study the detector performance. Simulated events were processed and reconstructed in the same manner as collision data. In this analysis, the following Monte Carlo simulated samples have been used. Fully simulated Madgraph+Pythia6 Z2, Herwig++ EE3C and Pythia8 4C samples in the official MC production:

```
QCD/HT-*To*_TuneZ2star_8TeV-madgraph-pythia/Summer12_DR53X-PU_S10_START53_V7A-v1
QCD/Pt-15to3000_TuneEE3C_Flat_8TeV_herwigpp/Summer12_DR53X-PU_S10_START53_V7A-v1
QCD/Pt-*to*_Tune4C_8TeV_pythia8/Summer12_DR53X-PU_S10_START53_V7A-v1/AODSIM
```

and privately generated particle-level Pythia6 Z2, Herwig++ and Pythia8 4C samples with significantly increased statistics using the official configurations.

A variety of comparisons were made between the data and simulation to verify that the simulation provided an adequate description of the QCD events observed in the data. We explore all mass regimes here. All the event selection requirements used in the final analysis have been applied to both MC and data. The MC distributions are normalized to the number of events in data.

The comparison plot for dijet invariant mass in data and MC is shown in Figure 2 for  $M_{jj}$ . In Figure 3 and 4 the  $p_T$  distributions are compared for both the leading and 2<sup>nd</sup>-leading jets in



the event in all mass bins. In Figures 5 and 6, the rapidities of the leading and 2<sup>nd</sup>-leading jets are plotted for all mass bins. In Figure 7, we compare the  $y_{boost}$  distribution in data and MC, in Figure 8, the  $\chi_{dijet}$  distribution, in Figure 9 the  $\frac{p_{T,1}-p_{T,2}}{p_{T,1}+p_{T,2}}$  distribution, in Figure 10,  $\Delta\phi_{1,2}$  distribution, and in Figure 11, the  $E_T^{miss} / \sum E_T$  distribution. The comparisons are shown for the resolution smeared Pythia Z2, Herwig++ and Pythia8 4C Monte Carlo. In general, there is reasonable agreement of data and MC. In most distributions, the data lies in between the predictions of Pythia Z2 and Herwig++.

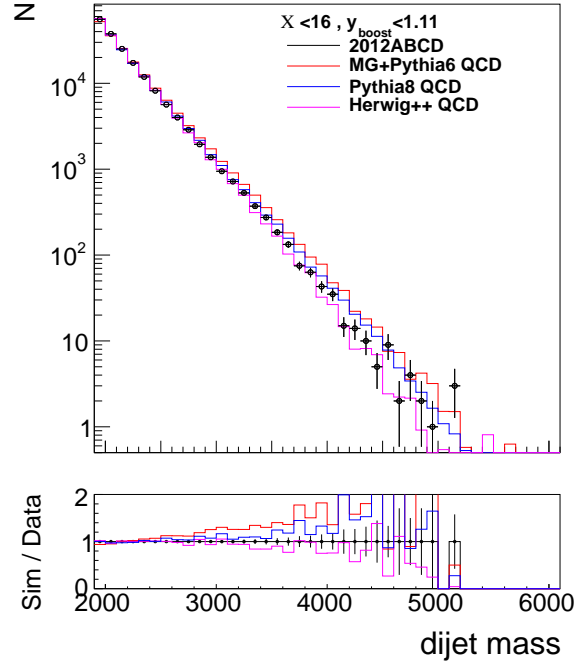


Figure 2: Comparisons of distributions in the dijet invariant mass between data (points) and simulation (histograms) for  $M_{jj}$ .

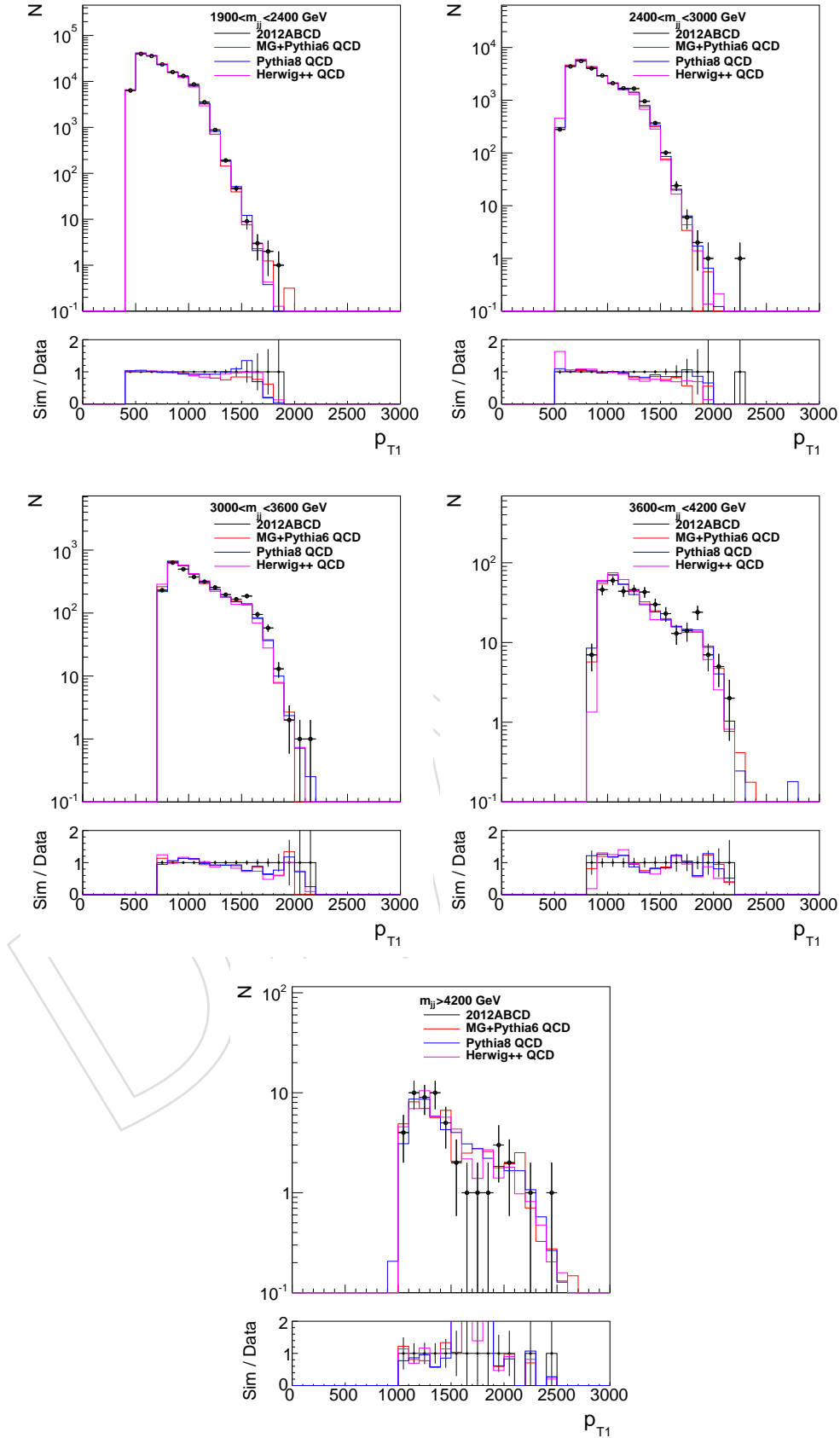


Figure 3: Comparisons of distributions in  $p_T$  for leading jet between data (points) and simulation (histograms).

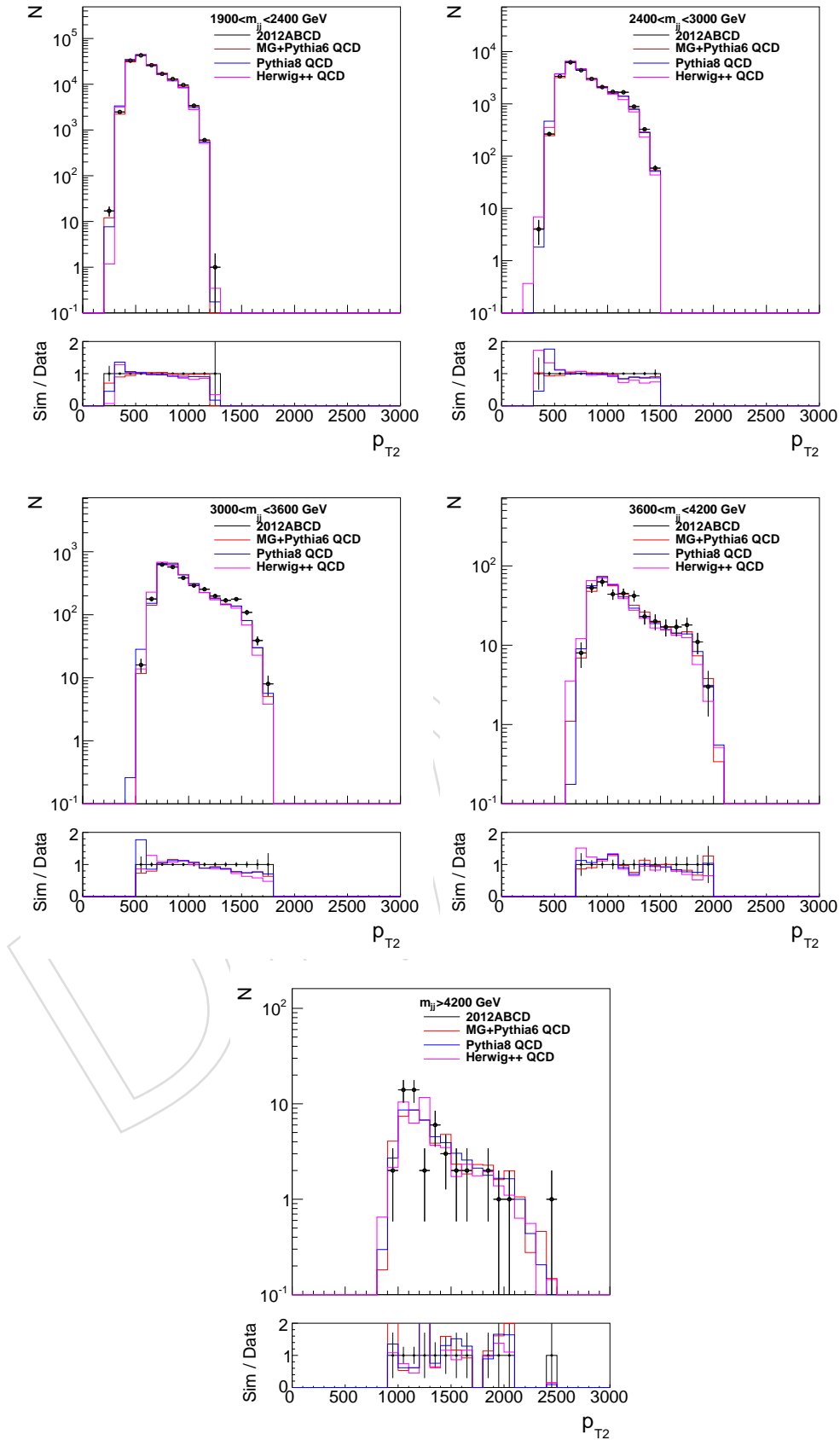


Figure 4: Comparisons of distributions in  $p_T$  for 2<sup>nd</sup> leading jet between data (points) and simulation (histograms).

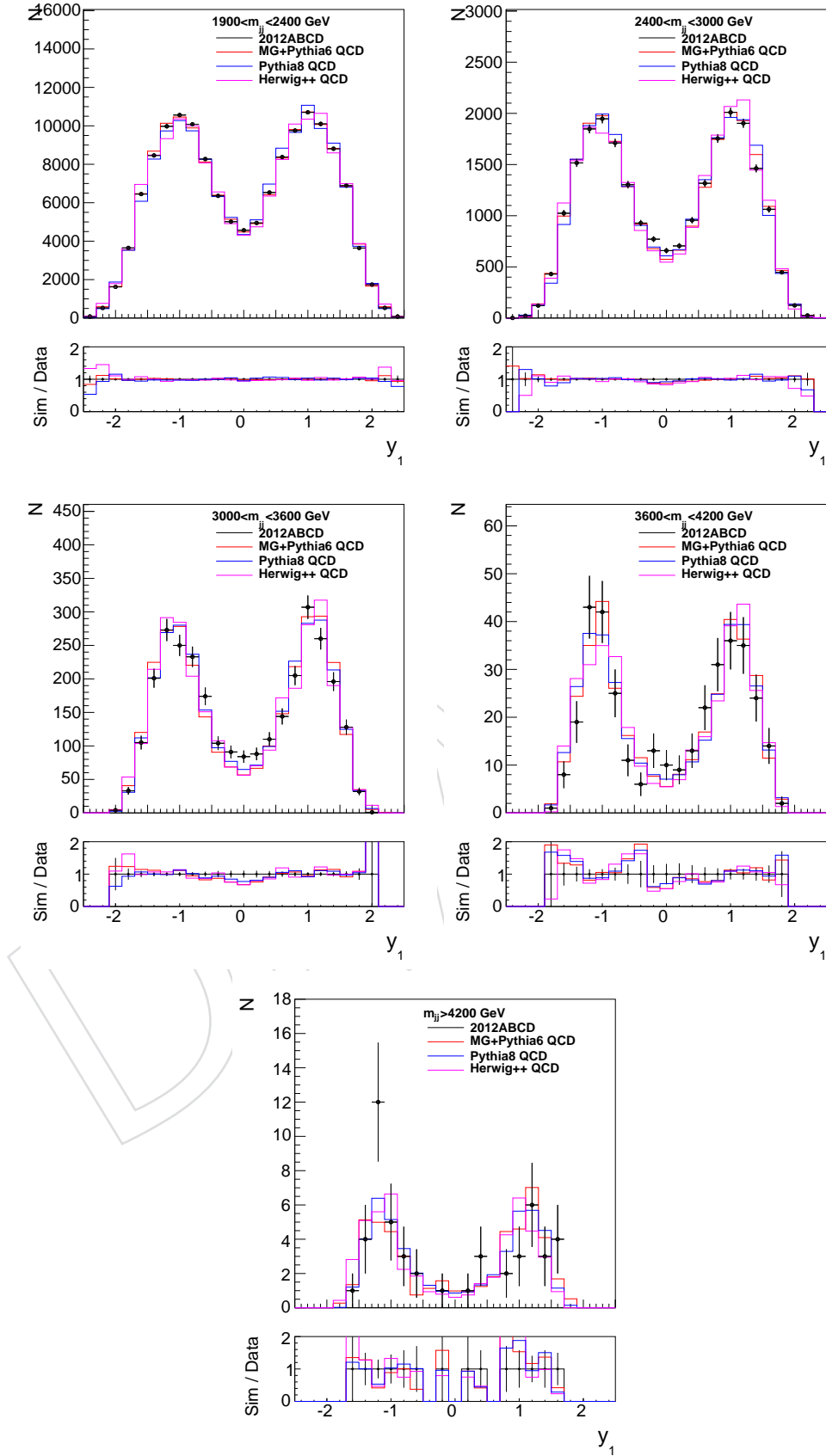


Figure 5: Comparisons of distributions in rapidity for leading jets between data (points) and simulation (histograms).

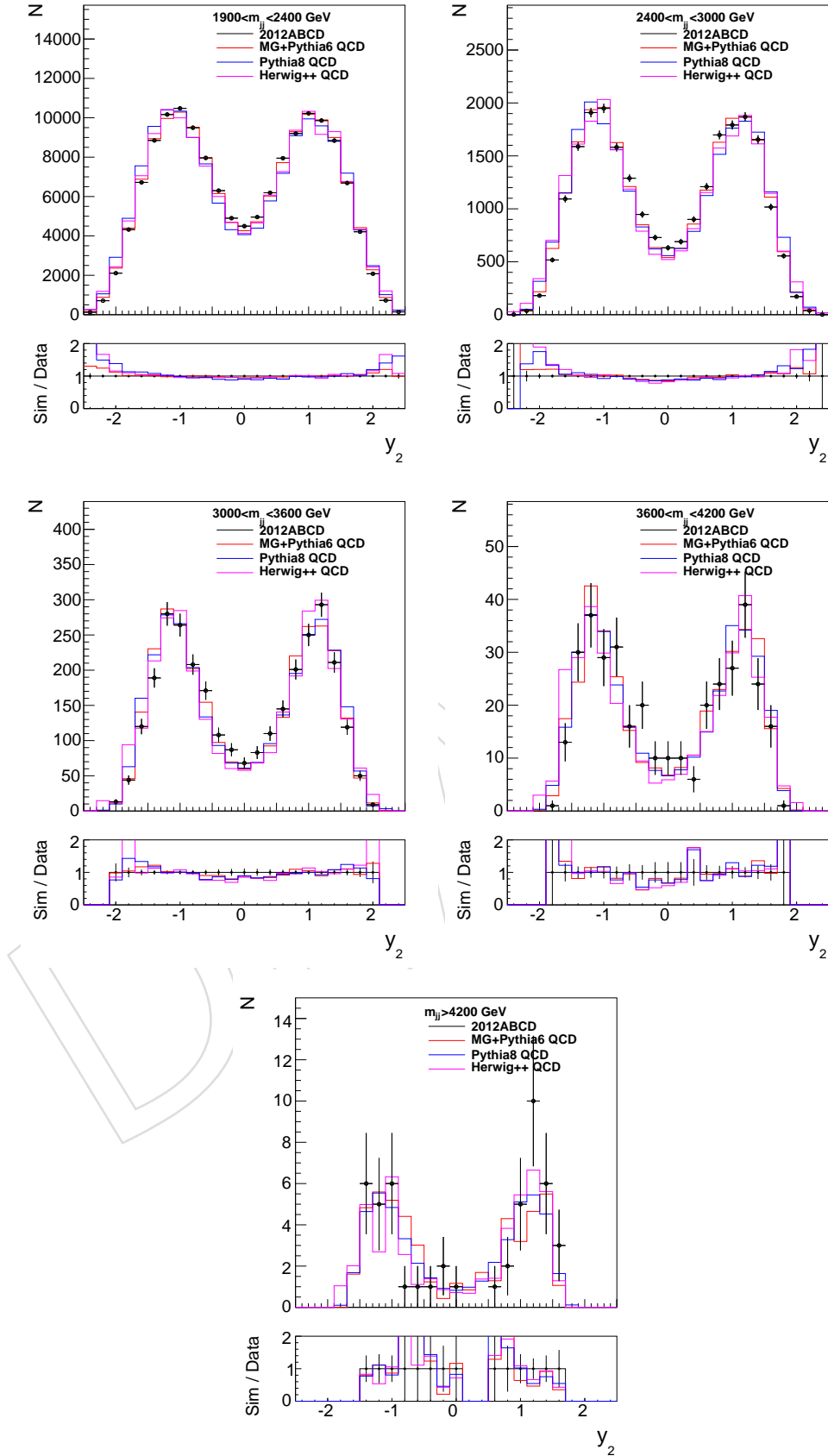


Figure 6: Comparisons of distributions in rapidity for 2<sup>nd</sup> leading jets between data (points) and simulation (histograms).

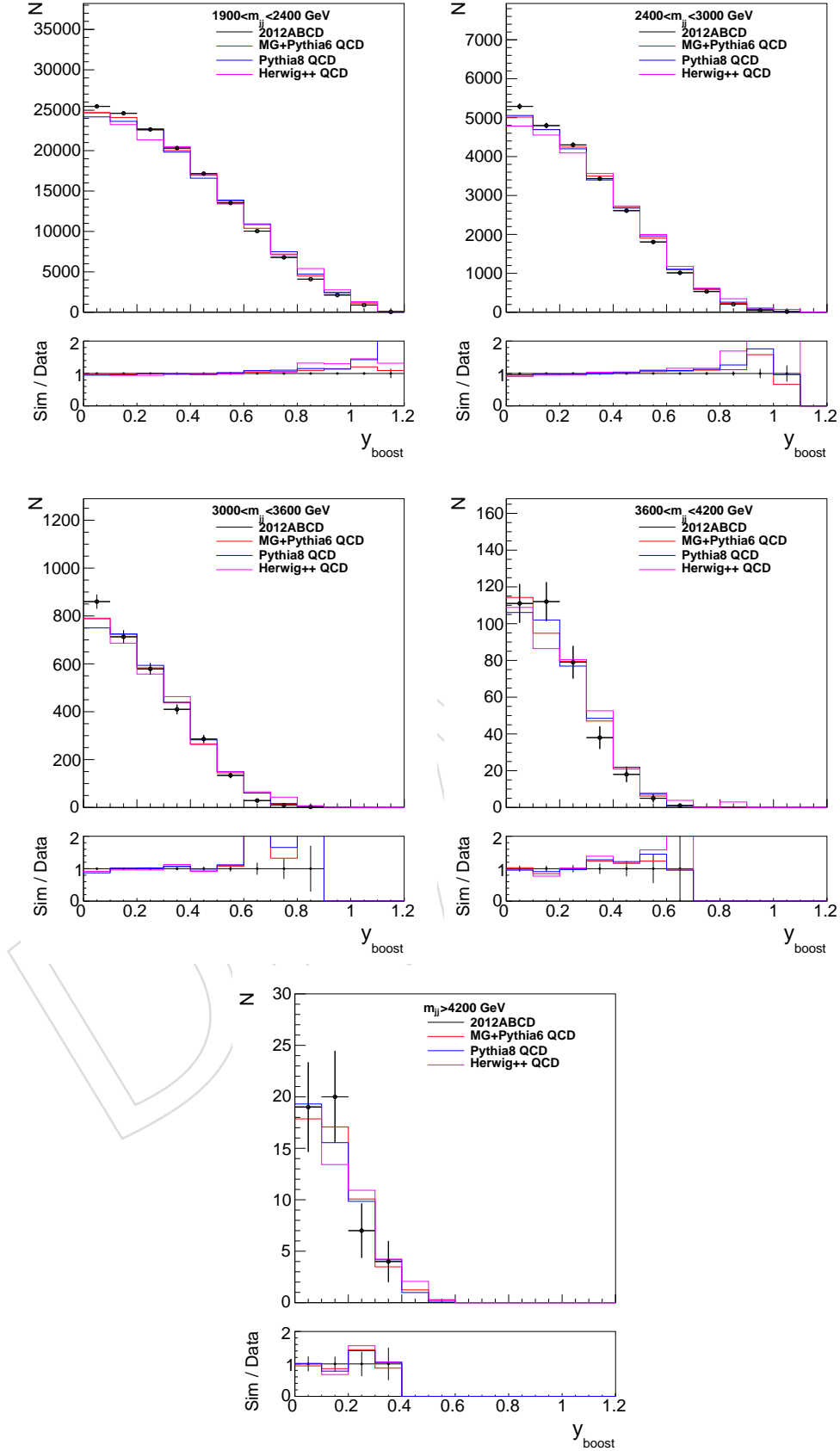
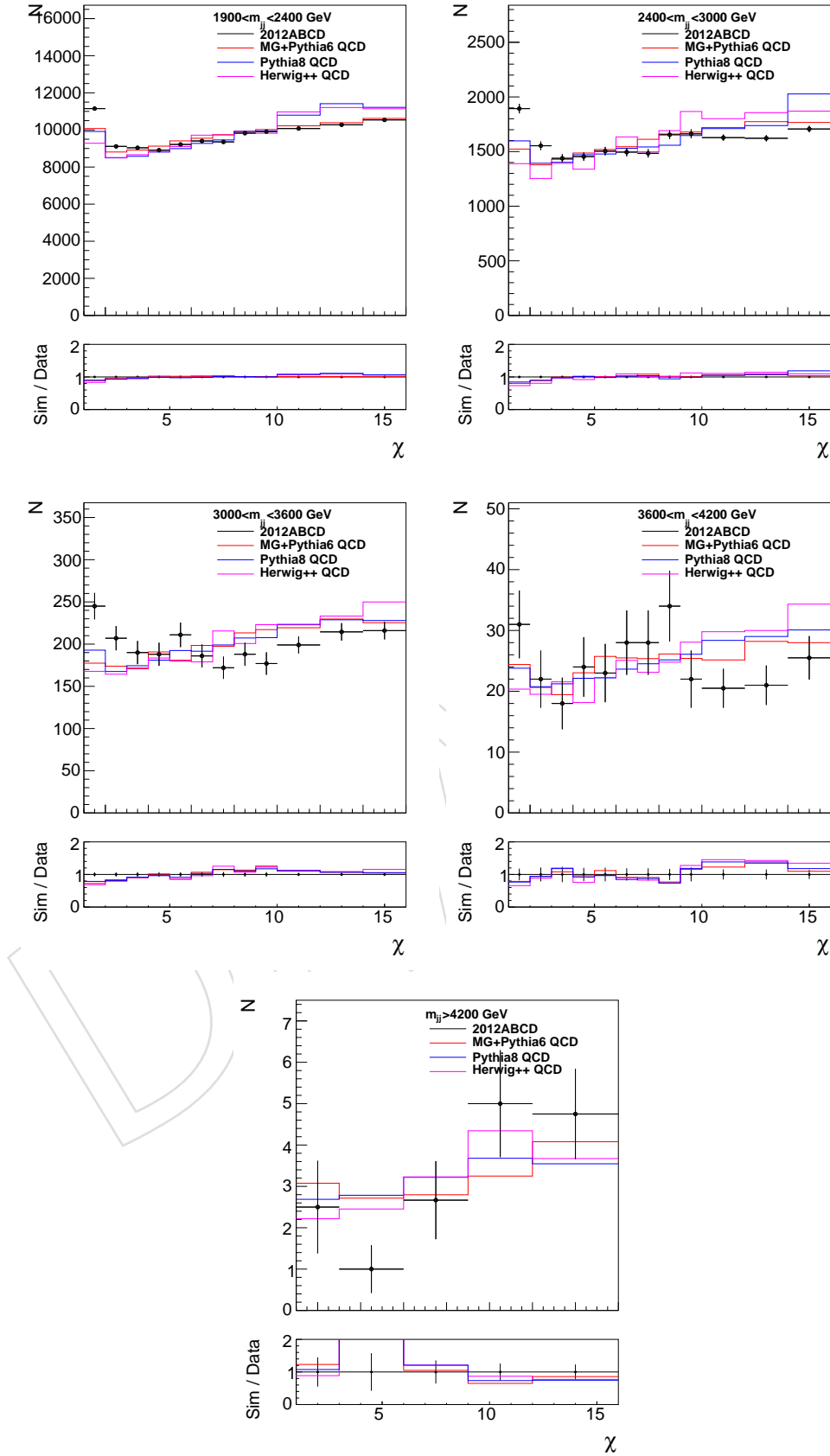


Figure 7: Comparisons of distributions in  $y_{\text{boost}}$  between data (points) and simulation (histograms).

Figure 8: Comparisons of distributions in  $\chi$  between data (points) and simulation (histograms).

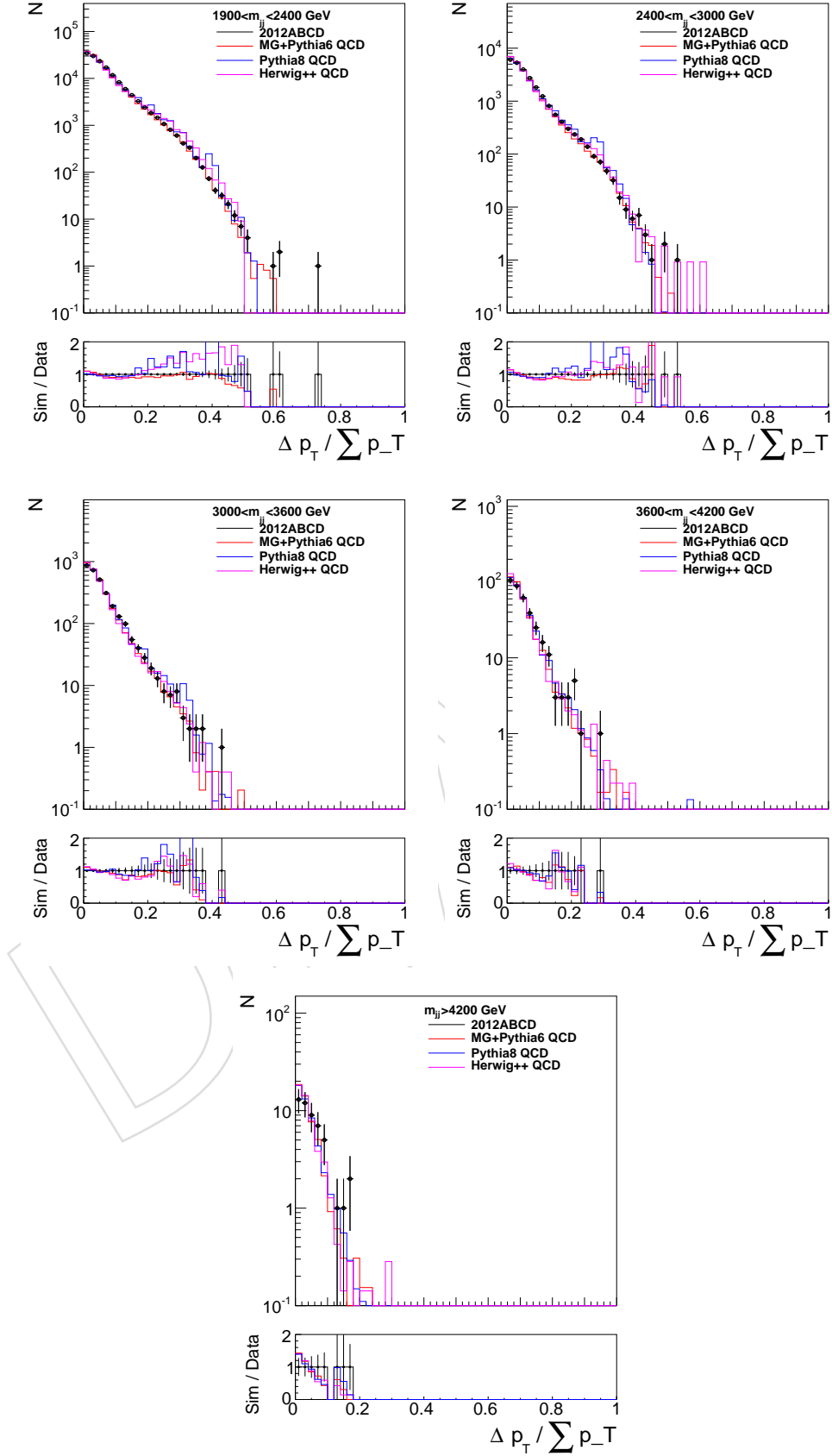


Figure 9: Comparisons of distributions in  $\frac{p_{T,1}-p_{T,2}}{p_{T,1}+p_{T,2}}$  between data (points) and simulation (histograms).



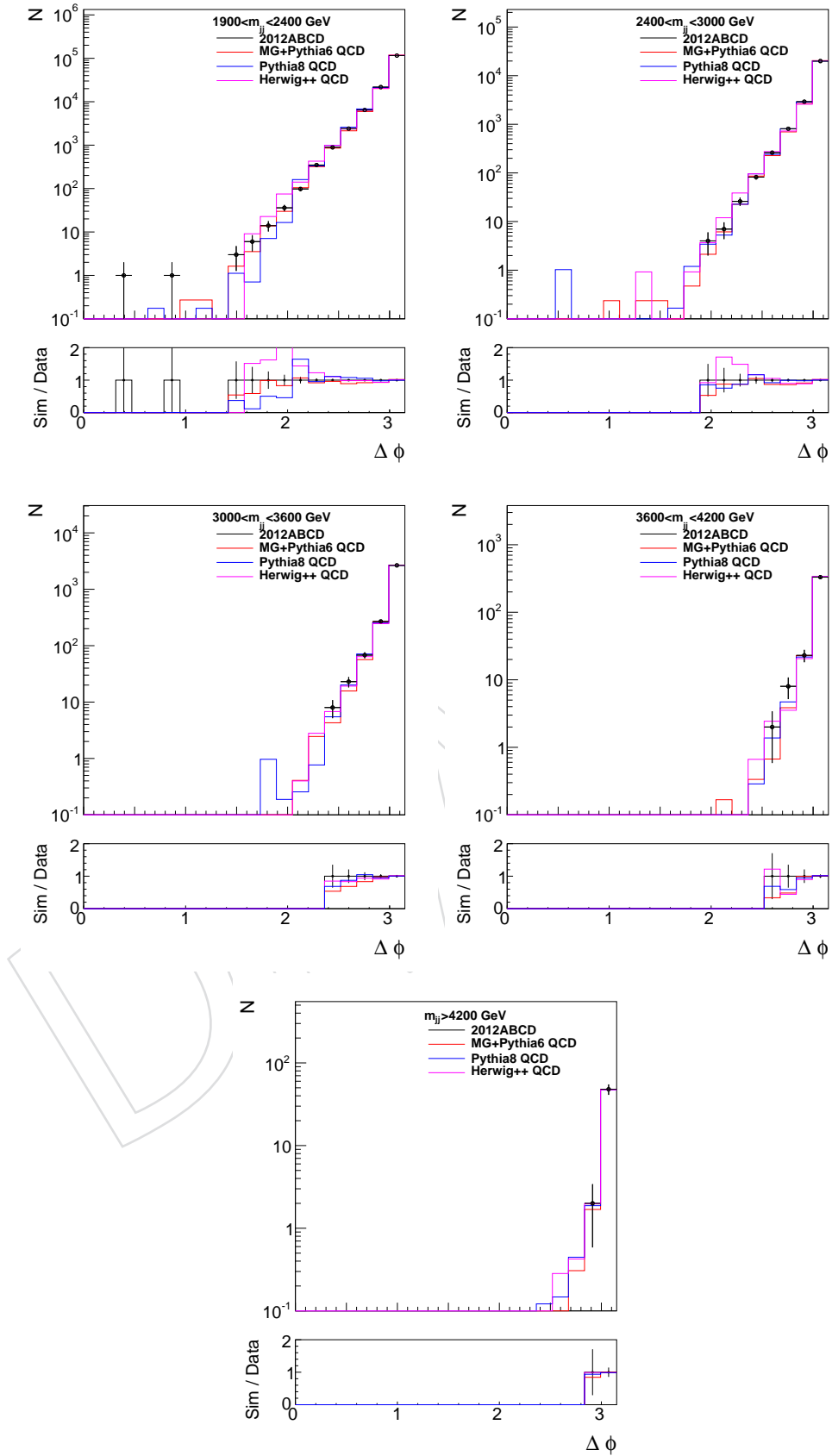


Figure 10: Comparisons of distributions in  $\Delta\phi_{1,2}$  between data (points) and simulation (histograms).

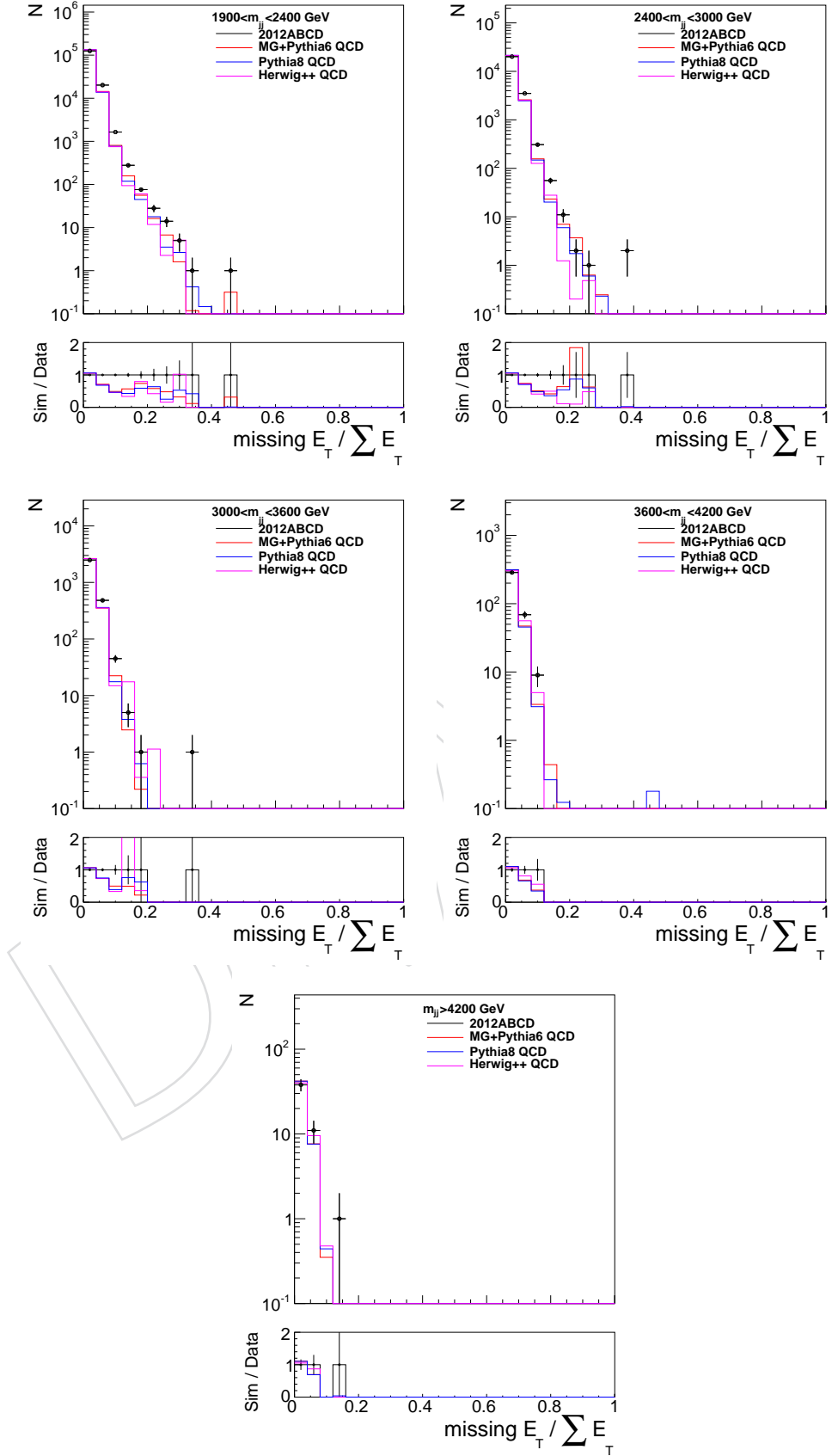


Figure 11: Comparisons of distributions in  $E_T^{\text{miss}} / \sum E_T$  between data (points) and simulation (histograms).

## 4.4 Detector Effects and Unfolding

In this section, we investigate the effects of the imperfect detector measurements on the dijet angular distributions. The largest effects are expected to come from jet energy resolution, which arise primarily from energy fluctuations due to electronic noise, pile-up, energy sampling, and from non-uniformities and non-linearities in the detector response, and jet position resolution.

In Figure 12, the jet  $p_T$  resolution from energy-corrected particle-flow jets from the full detector simulation and those from particle-level jets that were smeared in energy according to resolution functions that were derived by the JetMET POG [26, 29, 30] is shown. Two parametrizations of the detector resolution are compared, one with a simple Gaussian function and another with a double-sided Crystal-Ball function which adds tails to the Gaussian core resolution. The core resolution is well described by both parametrizations. The high end tail, which is important for this analysis due to the steeply falling dijet mass spectrum, is well described by the Crystal-Ball parametrization. In Figure 13, the dijet angular distributions from the GEANT simulation and Crystal-Ball parametrization are compared and found to be in good agreement, indicating that the bulk of the detector effects on the dijet angular distribution can be attributed to jet energy smearing.

The measured  $\chi_{dijet}$  distributions were corrected for migration effects due to the finite jet  $p_T$  resolution of the detector. Fluctuations in the jet response can cause event migrations between bins in  $\chi_{dijet}$  as well as in between bins of dijet mass, as fluctuations in the jet response can cause low energy jets to be misidentified as leading jets. We therefore perform a two dimensional unfolding in dijet mass and  $\chi_{dijet}$  using a Bayesian method [31] implemented in the RooUnfold package [32]. The response matrix used for the unfolding was filled using particle-level jets that were smeared using the double-sided Crystal-Ball function described earlier. Four iterations are used for the unfolding and it was checked that increasing the number of iterations up to 10 does not change the result. A closure test of the method was performed by splitting the simulated samples into independent training and testing samples. An unsmeared matrix was determined from the training sample and then used to unfold the  $\chi_{dijet}$  distributions from the testing sample. The results from the closure test are shown in Fig. 14 and no significant discrepancies were observed.

## 4.5 Systematic Uncertainties

The dominant sources of experimental uncertainty arises from the uncertainties in the jet energy scale (JES) and jet energy resolution (JER). The contributions to the total systematic uncertainty from each of these sources are described below.

### 4.5.1 Uncertainty due to the Jet Energy Scale

To calculate the uncertainty introduced by the uncertainty on the jet energy scale, the energy of the particle-flow jets is varied according the  $p_T$  and  $\eta$  dependent uncertainties on the various sources of uncertainty on the jet energy scale [26]. The  $\chi_{dijet}$  distributions are evaluated with the energy of all jets increased (decreased) according to  $p_T$  and  $\eta$  dependent uncertainties. Then the ratio between the  $\chi_{dijet}$  distributions for the original particle-flow jets and the ones with increased (decreased) jet energy is taken, as shown in Figure 15 and 16. All sources are combined to an overall uncertainty labeled "sum in quadrature" in Figure 17 which turns out to be larger than a simple overall variation of the jet energy scale ignoring the correlations of the various sources.

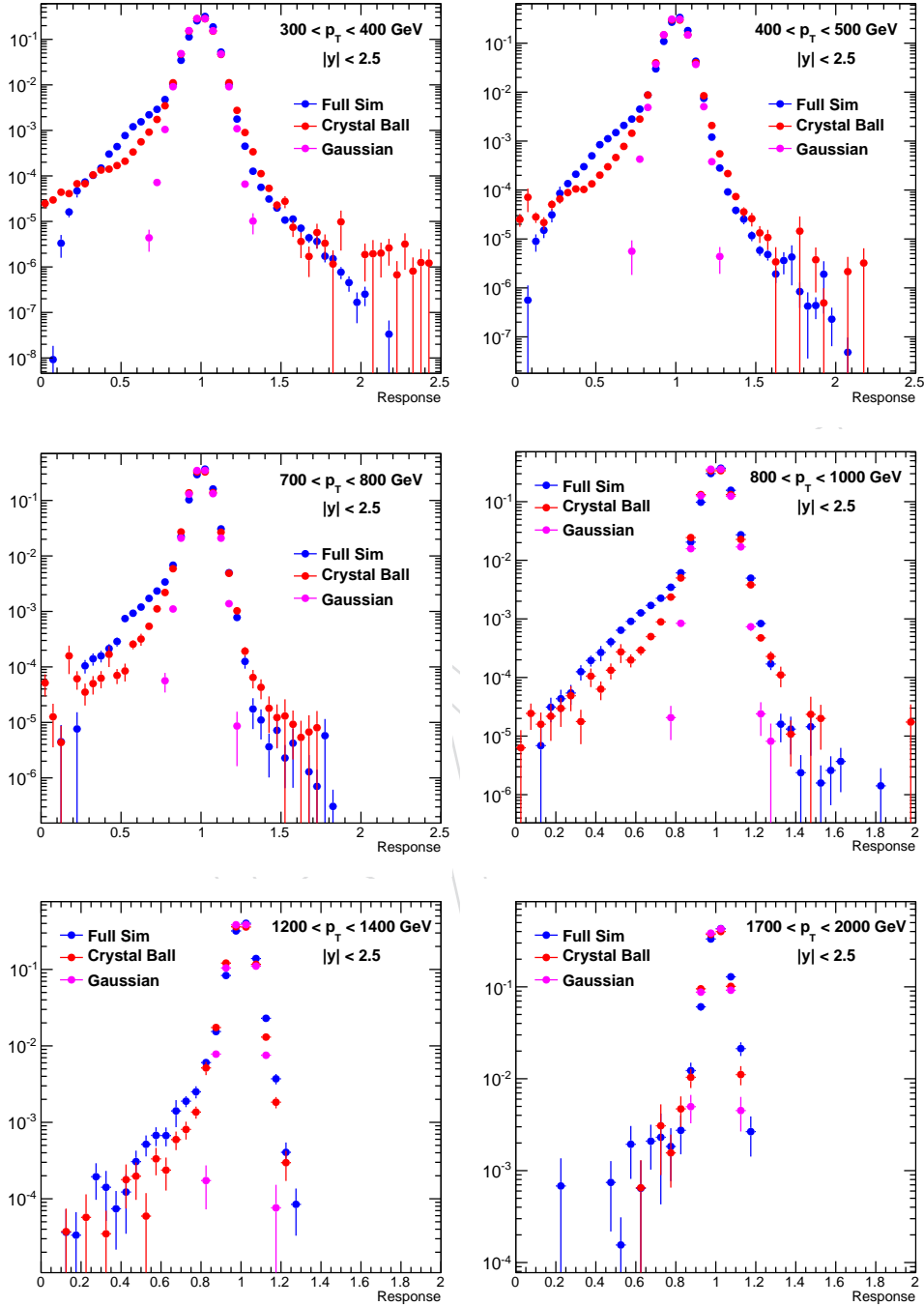


Figure 12: Jet  $p_T$  response from the GEANT detector simulation compared to the response from generated jets smeared with Gaussian and Crystal-Ball parameterizations of the jet resolution, for several bins in jet  $p_T$ .

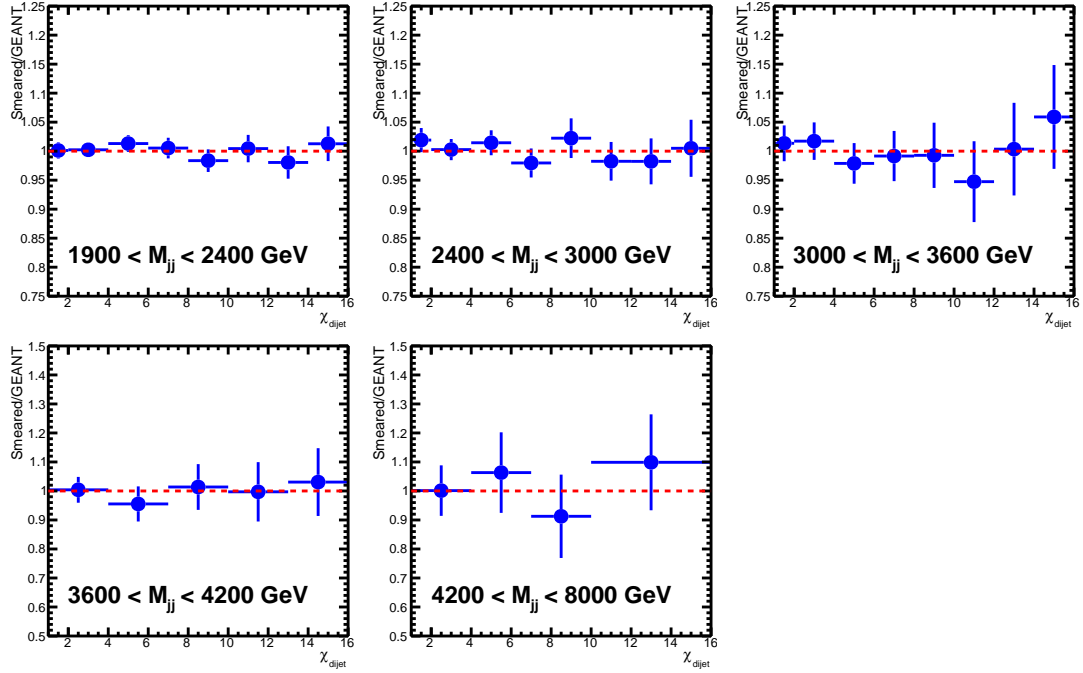


Figure 13: Dijet angular distributions ( $\chi_{dijet}$ ) from smeared generated jets compared to those from JES-corrected particle-flow jets from the GEANT full simulation.

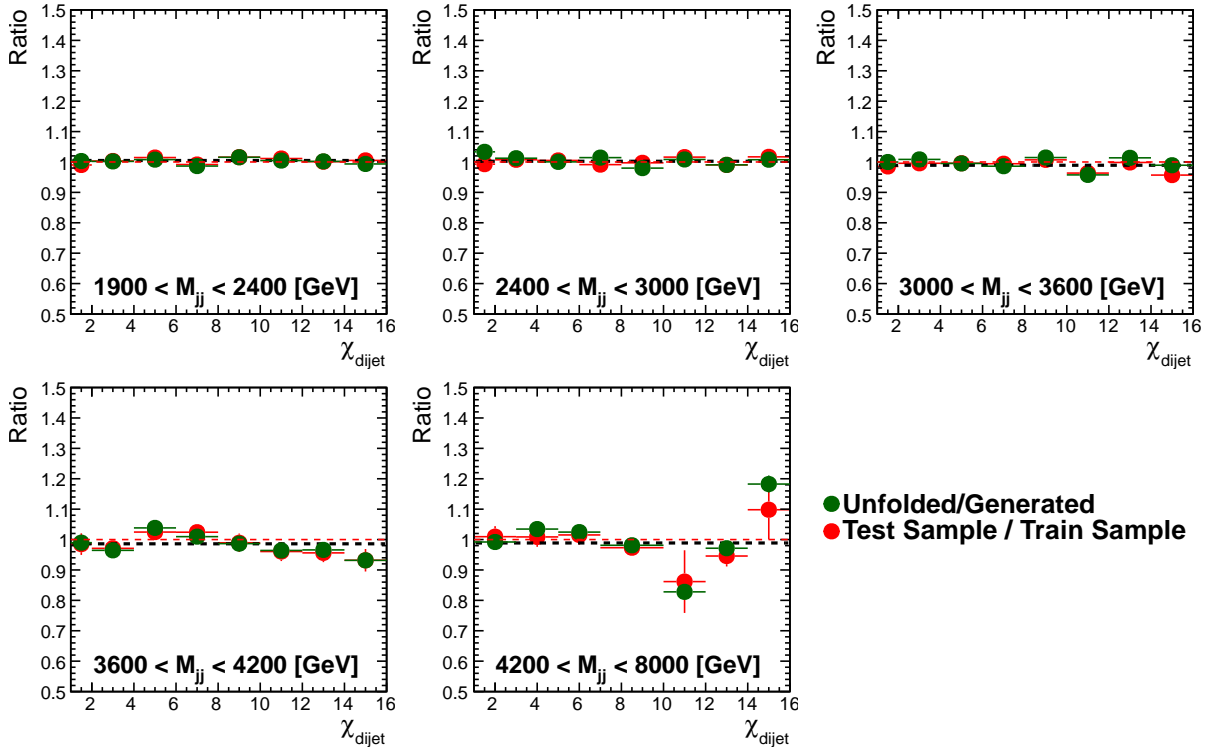


Figure 14: Ratios of unfolded and generated  $\chi_{dijet}$  distributions, where the unfolding correction was determined from an independent sample of events. Also shown are the ratios of the  $\chi_{dijet}$  distributions in the two samples to indicate the statistical differences in the samples.

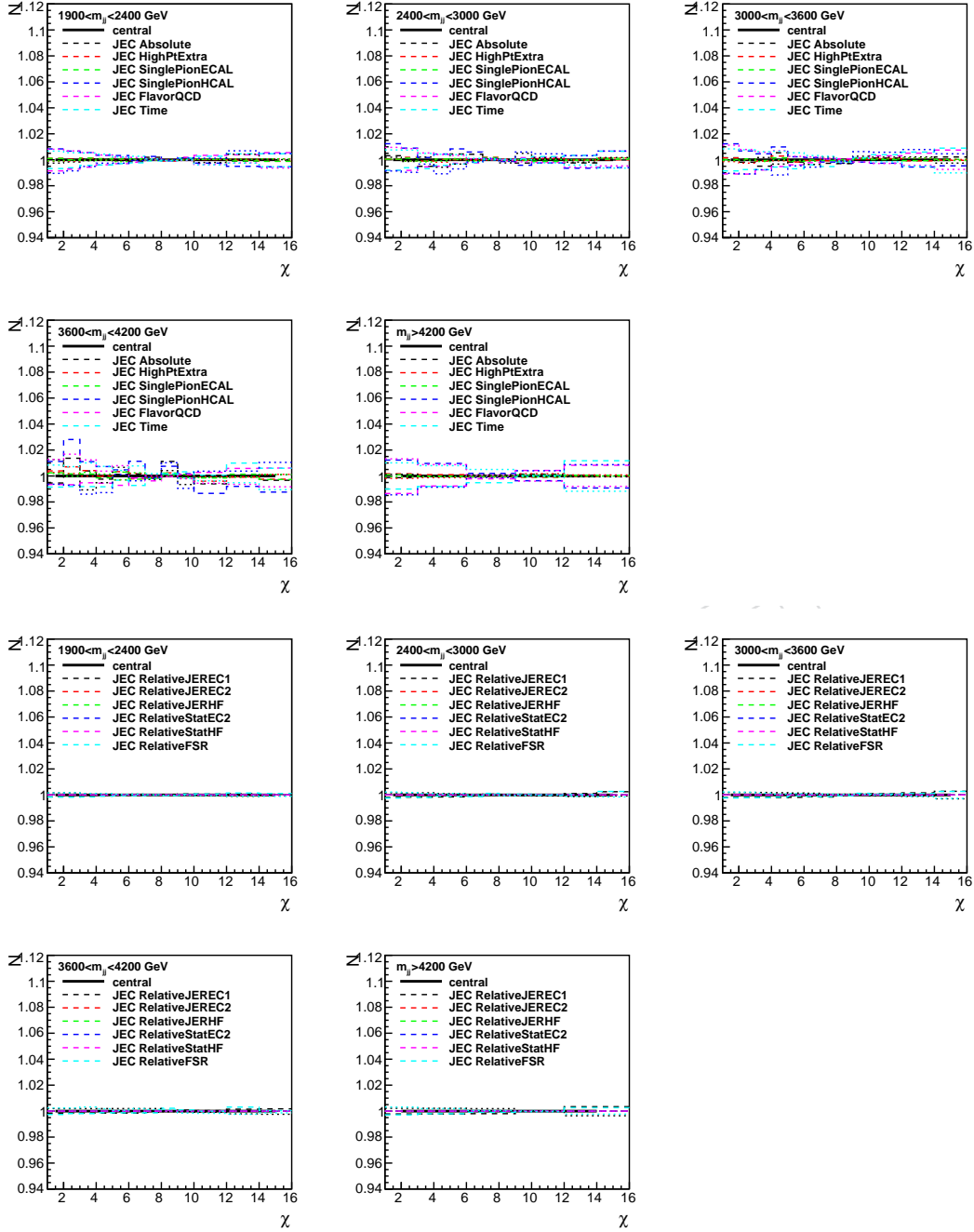


Figure 15: The effect of the jet energy correction uncertainty on the dijet angular distribution ( $\chi_{dijet}$ ).

#### 4.5.2 Uncertainty due to the Jet Energy Resolutions

For the jet energy resolution uncertainty, a variation of roughly 10% in the Gaussian core of the jet energy resolution function is considered [26]. To evaluate the effect of the jet energy resolution uncertainty on the dijet angular distributions, the generated jets are smeared in energy using Gaussians with widths given by the measured MC jet energy resolution. Additional jet collections are obtained by smearing the generated jets with jet energy resolution varied by  $\pm 10\%$  from the nominal values. The uncertainty is obtained from the ratios of the  $\chi_{dijet}$  distributions obtained with the  $\pm 10\%$  shift in the JER to those obtained from the nominal JER. These

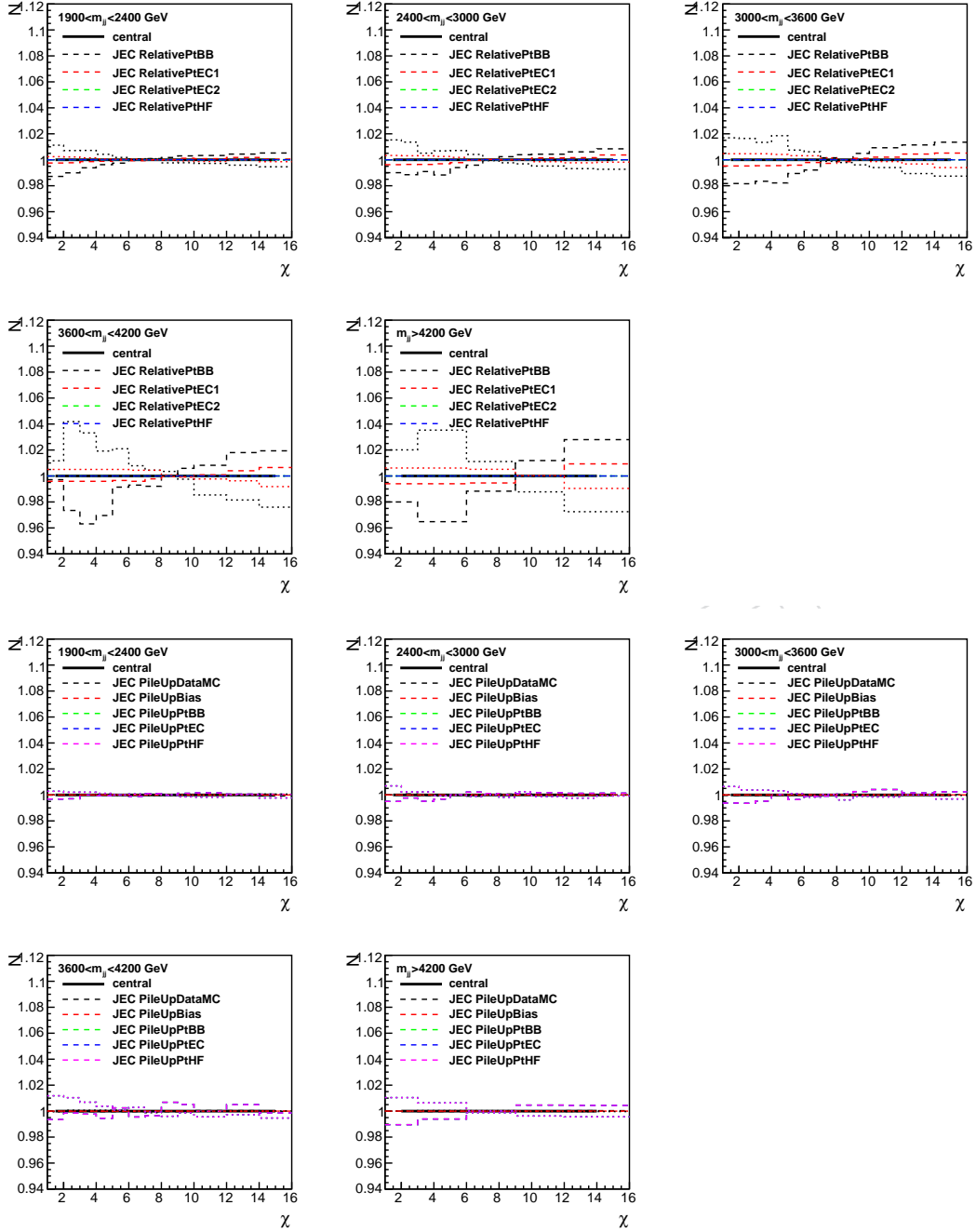


Figure 16: The effect of the jet energy correction uncertainty on the dijet angular distribution ( $\chi_{dijet}$ ).

ratios are shown in Fig. 18.

The unsmearing factor is derived taking into account the full jet energy resolution parametrization including tails. However, the size of the jet resolution tails has been constrained from data only to a limited extent [26]. Figure 19 shows the correction factor derived with and without tails. We assign 50% of this difference as an additional uncertainty.

Another source of systematic uncertainty considered comes from the fact that the smeared generator jets, used to derive the unfolding corrections, do not fully describe the detector ef-

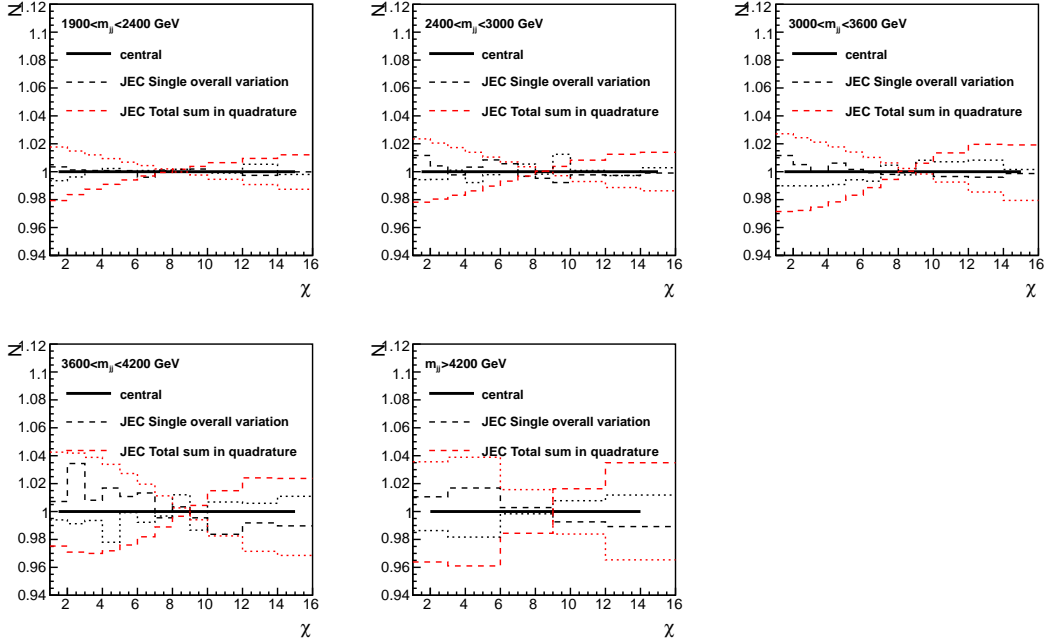


Figure 17: The effect of the jet energy correction uncertainty on the dijet angular distribution ( $\chi_{dijet}$ ).

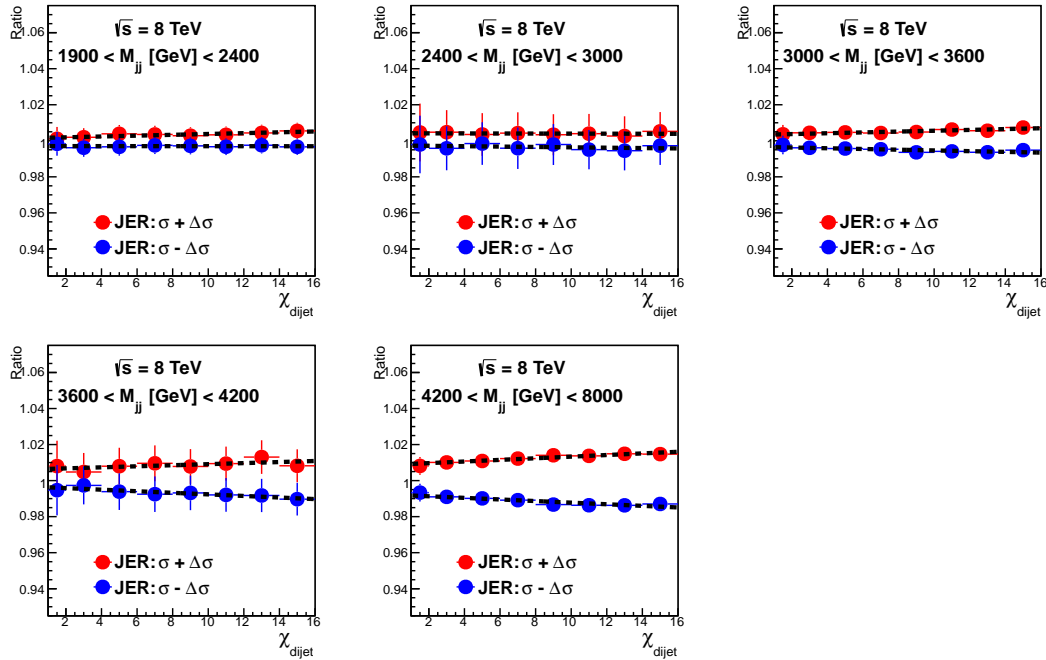


Figure 18: The effect of jet energy resolution uncertainty on the dijet angular distribution ( $\chi_{dijet}$ ).

fects. Therefore, the difference between smeared generated jets and JES-corrected reconstructed particle-flow jets from the GEANT simulation, as shown in Figure 13, is treated as an uncertainty.

Finally, we study the impact of using two different generators to derive the response matrix in Fig. 20. This probes the impact of possible mismodeling of the jet kinematics. The observed differences are much smaller than the uncertainties we assign for the jet energy resolution tails.



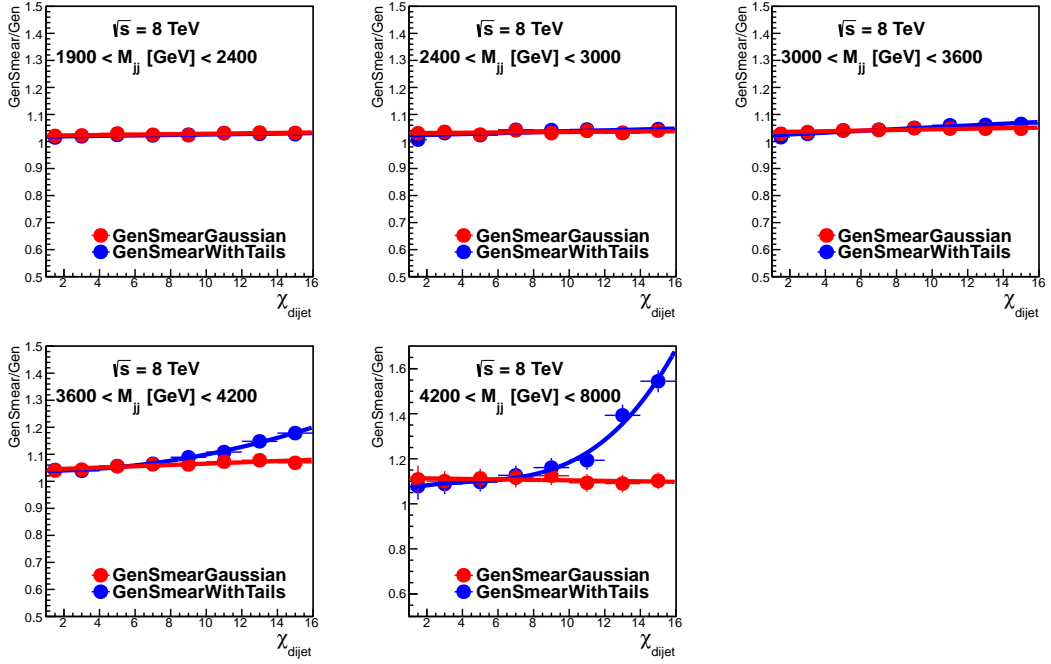


Figure 19: Effect of the jet energy resolution gaussian core (red) and tails (blue) on the smearing correction.

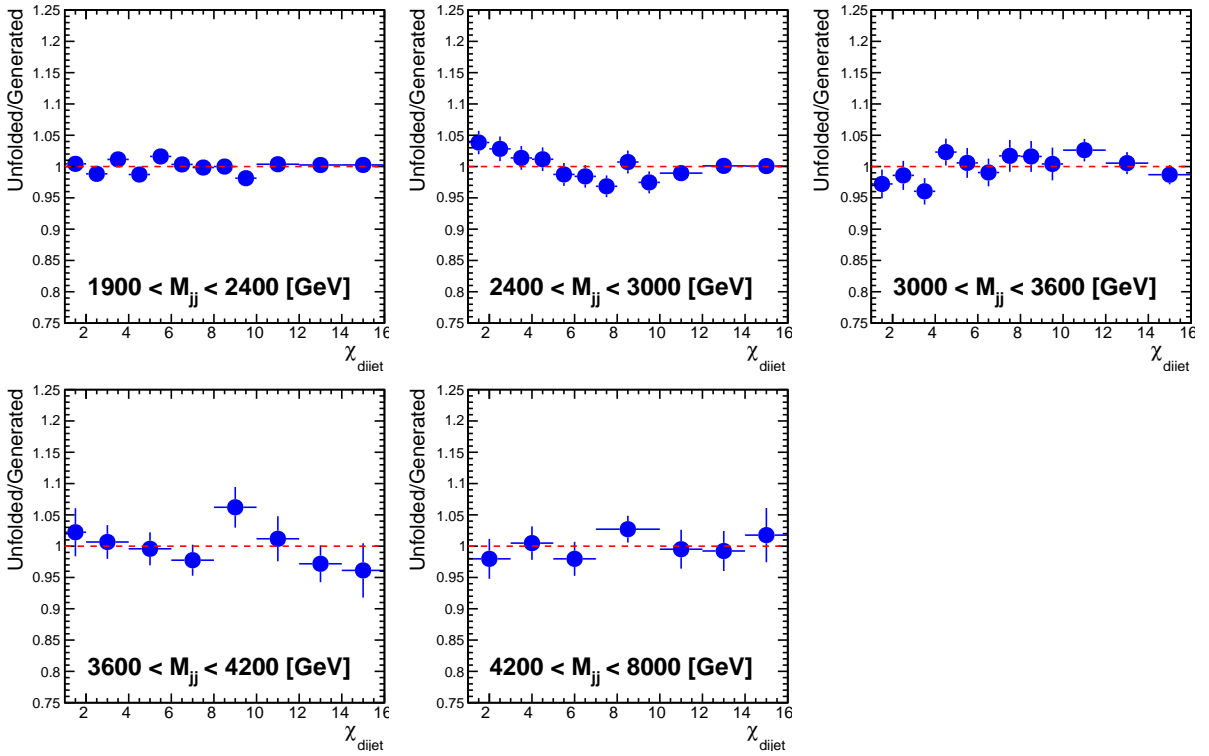


Figure 20: Ratios of unfolded and generated  $\chi_{dijet}$  distributions from PYTHIA where the response matrix used for the unfolding was derived from an independent sample of events generated by HERWIG.

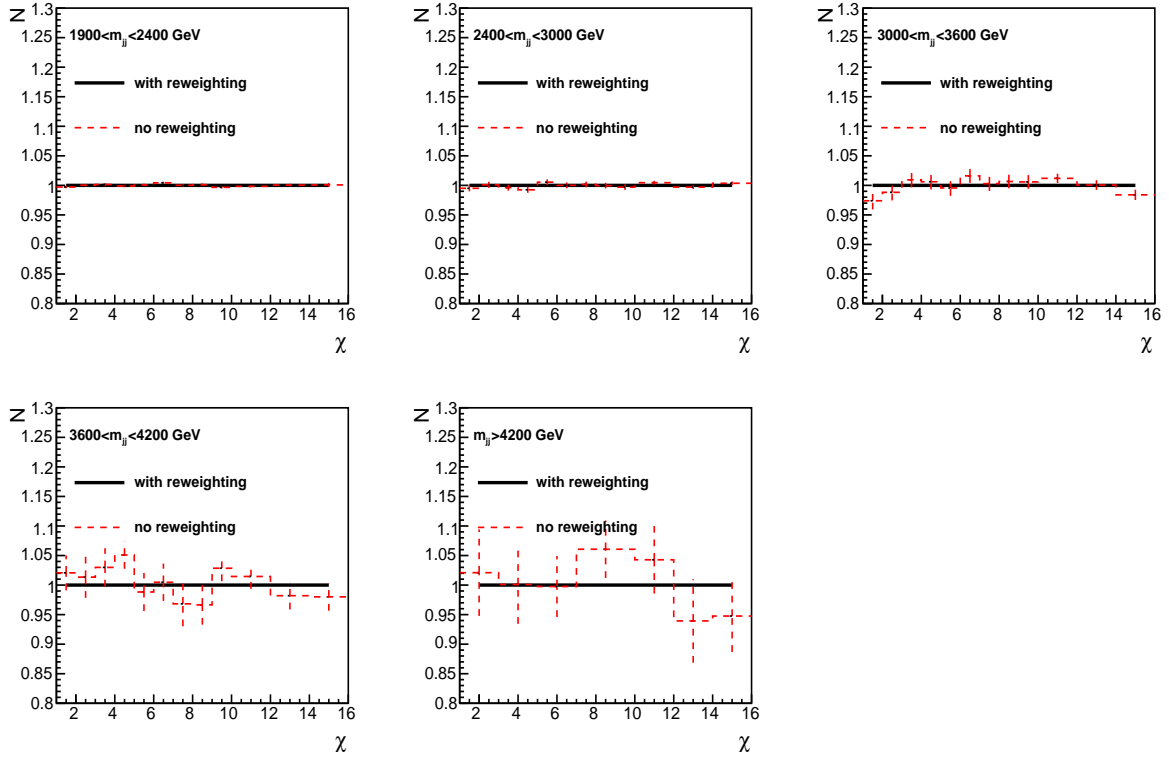


Figure 21: The ratio of the angular distributions with and without pileup reweighting.

## 4.6 Impact of pile up

At the LHC, the collisions overlapping in the same bunch-crossing is known as pile up. The impact of pile up is studied for the variable  $\chi$  with the base event selection. The detector simulation includes the simulation of pileup. The amount of pileup vertices is similar to the distribution data, though not perfect. Therefore a reweighting is applied to the simulated samples to match the pileup distribution of the 2012 data. We evaluate the sensitivity to pileup for this analysis by comparing the angular distributions with and without pileup reweighting in Fig. 21. This procedure is very similar to varying the cross section for pileup interactions according to its measured value, though yielding a slightly larger uncertainty estimate.

From the ratio of the angular distributions shown in Figure 21, the effect of pileup is found to be negligible.

## 5 Theory predictions

We use the NLOJET++ [33] program to calculate predictions for the angular distributions to next-to-leading order (NLO). This program is also integrated into the fastNLO package [34], which is used to calculate parton distribution function (PDF) and scale uncertainties with fast performance. A detailed description of the procedure is given in Ref [35]. The calculation is performed using CT10 NLO PDFs [36] with the same  $\alpha_S$  used in the matrix element calculation and in the PDFs. The factorization scale  $\mu_F$  and renormalization scales  $\mu_R$  are set to the average  $p_T$  of the two leading jets ( $\mu_F = \mu_R = \langle p_T \rangle$ ).

We use the same analysis phase space as defined in Section 2.

### 5.1 Non-perturbative corrections

To make meaningful comparisons, theory and data need to be compared at the particle-level. The NLO calculations, however, are performed at parton-level only. Therefore we derive non-perturbative corrections using Monte Carlo generators and apply them to the NLO predictions.

$$\sigma_{NLO+Non-Pert.}^{QCD} = \sigma_{NLO}^{QCD} \cdot (\text{non-perturbative corrections}) \quad (3)$$

We use PYTHIA8 and HERWIG++ to study the effect from different generators. The non-perturbative corrections are defined as the combination of the corrections due to hadronization (PartonLevel:MPI in PYTHIA8, LHCHandler:MultipleInteractionHandler in Herwig++) and to multiple parton interactions (HadronLevel:Hadronize in PYTHIA8, LHCHandler:HadronizationHandler in Herwig++). The resulting correction factors are shown in Figure 22. They are consistent with zero within the generated MC statistics for each mass bin. Therefore no correction is applied and no uncertainty is assigned.

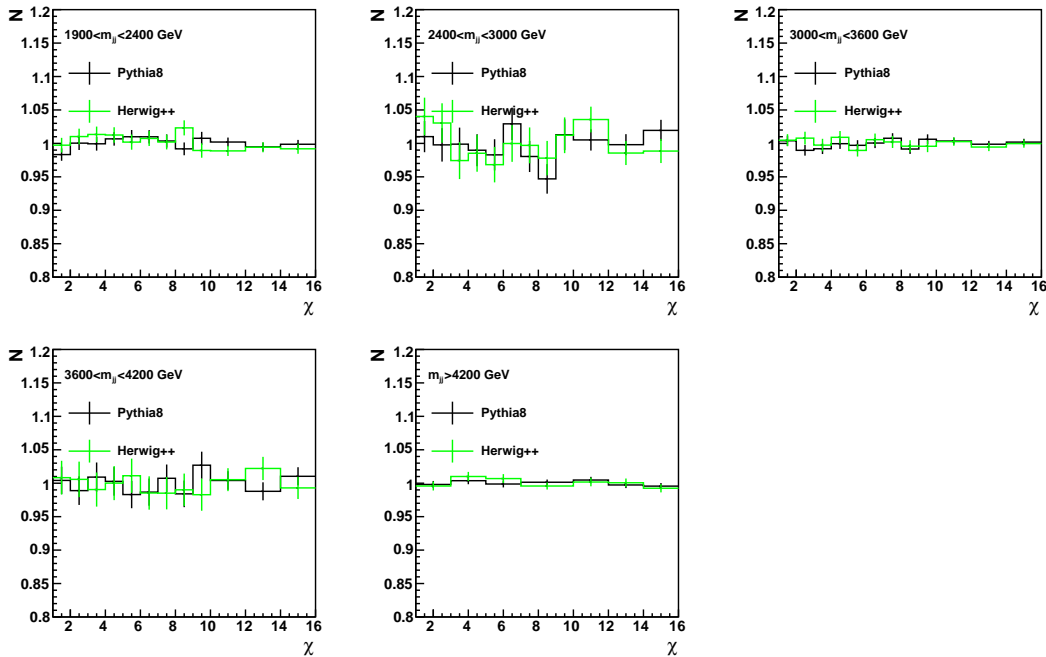


Figure 22: Non-perturbative corrections derived from PYTHIA8 (black) and HERWIG++ (green).

## 5.2 Systematic Uncertainties

The scale uncertainties are obtained by varying both  $\mu_F$  and  $\mu_R$  in six combinations:  $(\mu_f, \mu_r) = (\langle p_T \rangle/2, \langle p_T \rangle/2), (\langle p_T \rangle/2, \langle p_T \rangle), (\langle p_T \rangle, \langle p_T \rangle/2), (2\langle p_T \rangle, 2\langle p_T \rangle), (2\langle p_T \rangle, \langle p_T \rangle)$  and  $(\langle p_T \rangle, 2\langle p_T \rangle)$ . They are presented in Figure 23 (red dashed line). The scale uncertainty varies from 6% in the lowest mass bin, to 15% in the highest mass bin.

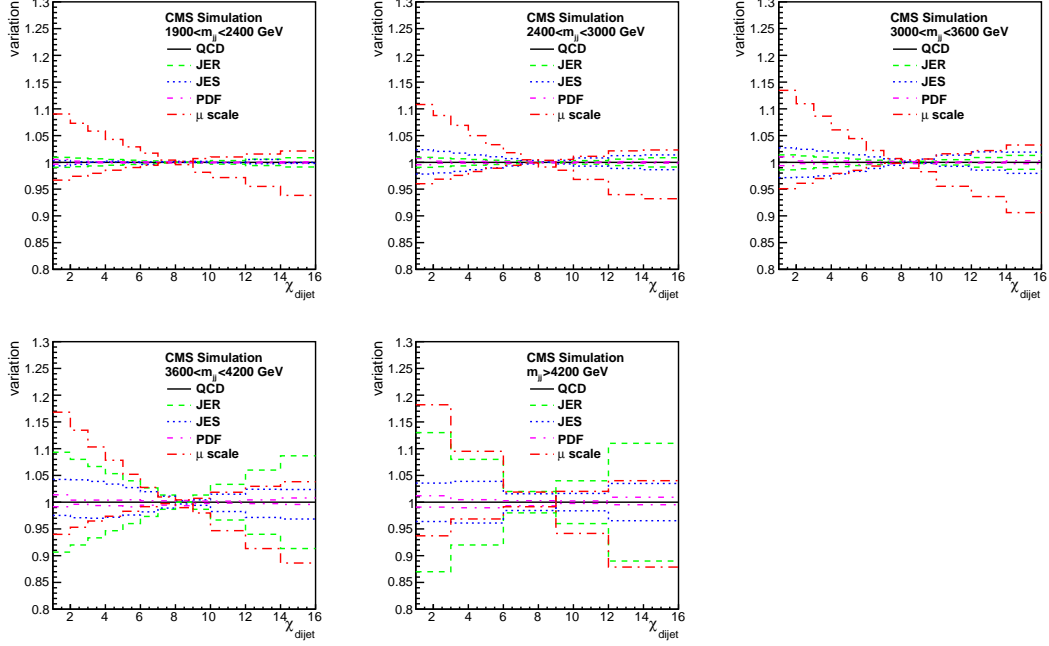


Figure 23: Scale and PDF uncertainty of the QCD NLO prediction.

The uncertainty in the calculation due to the PDF uncertainty were evaluated using the set of uncertainty eigenvectors provided with the CT10 PDF set. They are presented in Figure 23.

The statistical uncertainty for the NLO prediction is within  $\pm 1\%$  and neglected.

## 5.3 Contact Interaction predictions

This section describes the calculation of a generic new physics model with a Contact Interaction (CI) additional to QCD interactions. A Contact Interaction is introduced for quarks at an energy scale  $\Lambda$ . The corresponding effective Lagrangian for color-singlet contact interactions between quarks is

$$L_{qq} = \frac{g^2}{2\Lambda^2} [\eta_{LL}(\bar{q}_L \gamma^\mu q_L)(\bar{q}_L \gamma_\mu q_L) + \eta_{RR}(\bar{q}_R \gamma^\mu q_R)(\bar{q}_R \gamma_\mu q_R) + 2\eta_{RL}(\bar{q}_R \gamma^\mu q_R)(\bar{q}_L \gamma_\mu q_L).] \quad (4)$$

Color-octet contact interactions of similar form are not regarded in this analysis. Different combinations of  $\eta_{LL}$ ,  $\eta_{RR}$  and  $\eta_{RL}$  allow to construct different contact interaction models which are summarized in Table 3.

Note that for dijet production in pp collisions,  $\Lambda_{LL}^\pm = \Lambda_{RR}^\pm$ ,  $\Lambda_V^\pm = \Lambda_A^\pm$  and  $\Lambda_{V-A}^+ = \Lambda_{V-A}^-$ .

Both NLO and LO predictions are of interest. While the NLO predictions are at the state-of-the-art, the LO predictions are important for comparisons with older results, since the NLO predictions only became available recently [37].

Table 3: Mapping of contact interaction model and parameters.

model	$\eta_{LL}$	$\eta_{RR}$	$\eta_{RL}$
$\Lambda_{LL}^+$	1	0	0
$\Lambda_{LL}^-$	-1	0	0
$\Lambda_{RR}^+$	0	1	0
$\Lambda_{RR}^-$	0	-1	0
$\Lambda_V^+$	1	1	1
$\Lambda_V^-$	-1	-1	-1
$\Lambda_A^+$	1	1	-1
$\Lambda_A^-$	-1	-1	1
$\Lambda_{(V-A)}^+$	0	0	1
$\Lambda_{(V-A)}^-$	0	0	-1

298 The NLO predictions are calculated using the formalism described in Ref. [37] using the CT10  
 299 PDFs. These calculations include the contact interaction term as well as the interference terms  
 300 with QCD. The full prediction is obtained by adding the NLO QCD prediction.

Table 4: Pythia8 parameters for the generation of contact interactions.

parameter	value	description
HardQCD:gg2gg	on	processes as in QCD
HardQCD:gg2qqbar	on	processes as in QCD
HardQCD:qg2qq	on	processes as in QCD
HardQCD:qqbar2gg	on	processes as in QCD
HardQCD:gg2ccbar	on	processes as in QCD
HardQCD:qqbar2ccbar	on	processes as in QCD
HardQCD:gg2bbbar	on	processes as in QCD
HardQCD:qqbar2bbbar	on	processes as in QCD
HardQCD:qq2qq	off	processes with contact interactions
HardQCD:qqbar2qqbarNew	off	processes with contact interactions
ContactInteractions:QCqq2qq	on	processes with contact interactions
ContactInteractions:QCqqbar2qqbar	on	processes with contact interactions
ContactInteractions:nQuarkNew	5	Contact interactions between 5 quarks flavors
ContactInteractions:Lambda	$\Lambda$	Contact interaction scale in GeV
ContactInteractions:etaLL	$\eta_{LL}$	helicity for LL interactions
ContactInteractions:etaRR	$\eta_{RR}$	helicity for RR interactions
ContactInteractions:etaLR	$\eta_{RL}$	helicity for LR interactions

The LO predictions are calculated with PYTHIA8 using the CTEQ6L1 PDFs and the parameters given in Table 4. In order to obtain the best estimate for the QCD plus Contact Interaction process, we add the difference  $\sigma_{NLO}^{QCD} - \sigma_{LO}^{QCD}$  bin-by-bin to the Contact Interaction prediction and apply non-perturbative corrections:

$$\sigma^{QCD+CI} = (\sigma_{NLO}^{QCD} - \sigma_{LO}^{QCD} + \sigma_{LO}^{QCD+CI}) \cdot (\text{non-perturbative corrections}) \quad (5)$$

301 In the limit of  $\Lambda = \infty$  this formula yields the QCD prediction. Otherwise it yields the NLO QCD  
 302 prediction with the LO Contact Interaction term added. Note that the LO PYTHIA prediction  
 303 uses the CTEQ6L1 LO PDF while the NLO predictions use the CT10 NLO PDF.

Figures 24, 25 and 26 show predictions for angular distributions for several contact interaction models.

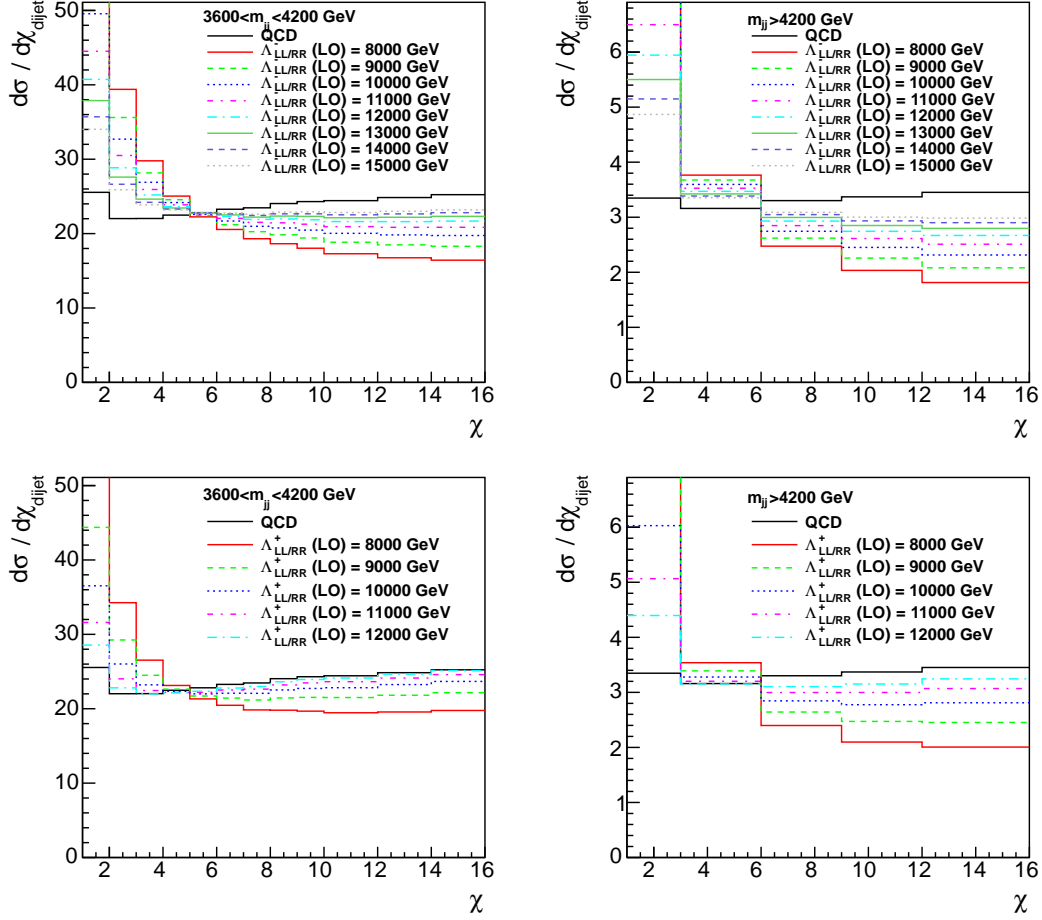


Figure 24: Theory prediction of the angular distributions for different contact interaction models.

#### 5.4 ADD predictions

The LO predictions for the ADD model in the GRW convention are calculated with PYTHIA8 using the CTEQ6L1 PDFs and the parameters given in Table 5. They are treated in the same way as the LO contact interaction prediction and corrected with the difference  $\sigma_{NLO}^{QCD} - \sigma_{LO}^{QCD}$ .

Table 5: Pythia8 parameters for the generation of ADD virtual graviton exchange.

parameter	value	description
HardQCD:all	off	custom dijet processes
ExtraDimensionsLED:dijets	on	use extra dimensions
ExtraDimensionsLED:CutOffmode	0	GRW convention
ExtraDimensionsLED:LambdaT	$\Lambda_T$	energy scale parameter
ExtraDimensionsLED:nQuarkNew	5	outgoing mass-less quark flavours
ExtraDimensionsLED:opMode	1	use GRW convention

Figure 27 show predictions for angular distributions for the ADD models.

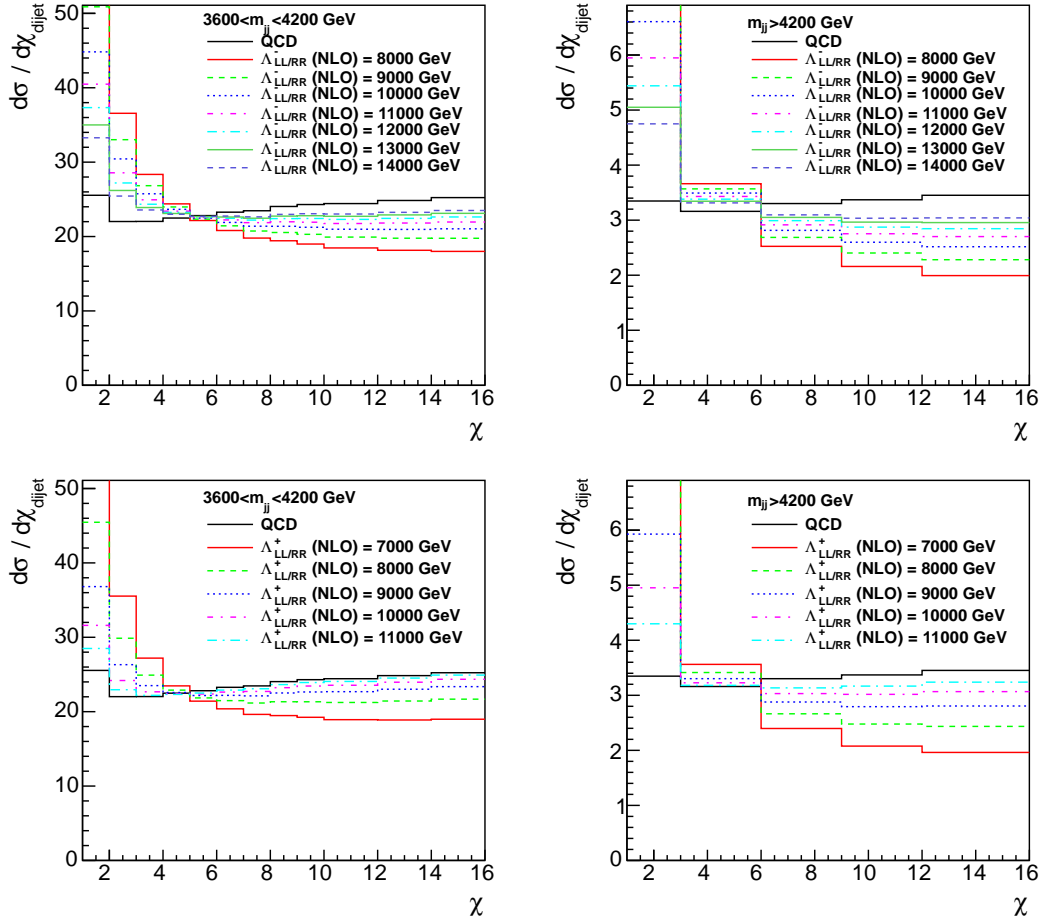


Figure 25: Theory prediction of the angular distributions for different contact interaction models.

311 The limits set on the GRW predictions can be translated to the HLZ convention with  $M_S =$   
 312  $\Lambda_T((n_{ED} - 2)/2)^{1/4}$  for  $n_{ED} > 2$ . For  $n_{ED} = 2$  the HLZ prediction can be assembled from the  
 313 GRW predictions using  $M_S = \Lambda_T(\ln(M_S^2/s))^{1/4}$ .

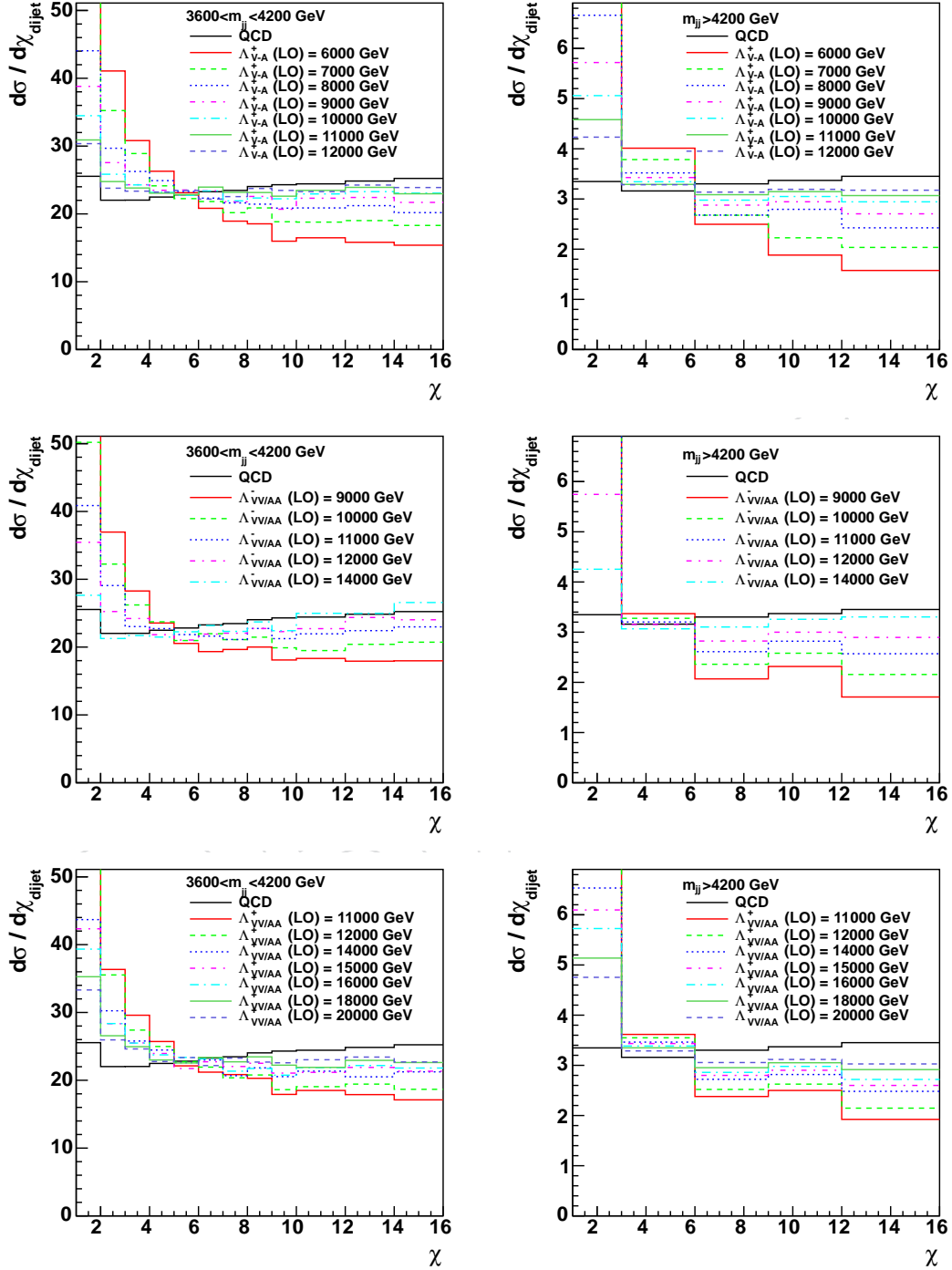


Figure 26: Theory prediction of the angular distributions for different contact interaction models.



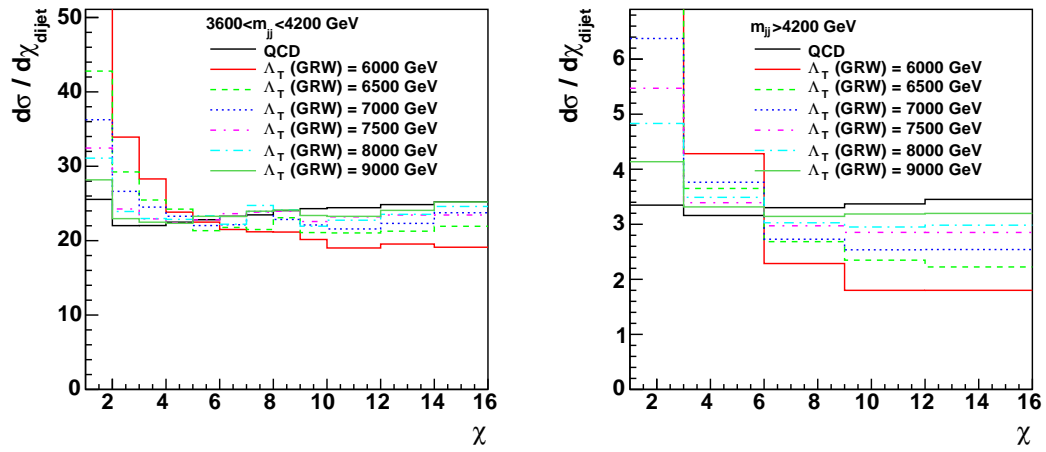


Figure 27: Theory prediction of the angular distributions for the ADD models.

## 6 Results

In Figure 28, the corrected dijet angular distributions, normalized to the total number of events within each  $M_{jj}$  region, are shown. The number of events in each mass bin are given in Table 2. The error bars in the final distributions reflect the statistical and systematic uncertainties added in quadrature.

The data are compared to pQCD predictions at next-to-leading order (NLO). Non-perturbative corrections due to hadronization and multiple parton interactions are applied to the NLO predictions. The factorization and renormalization scales are added in quadrature with the PDF uncertainties and the non-perturbative correction uncertainty. Overall there is good agreement between the theoretical prediction and the data.

In Figure 29, the data distributions for the two highest mass bins are compared to various CI and ADD models.

A summary of the statistical and systematic uncertainties can be found in Table 6.

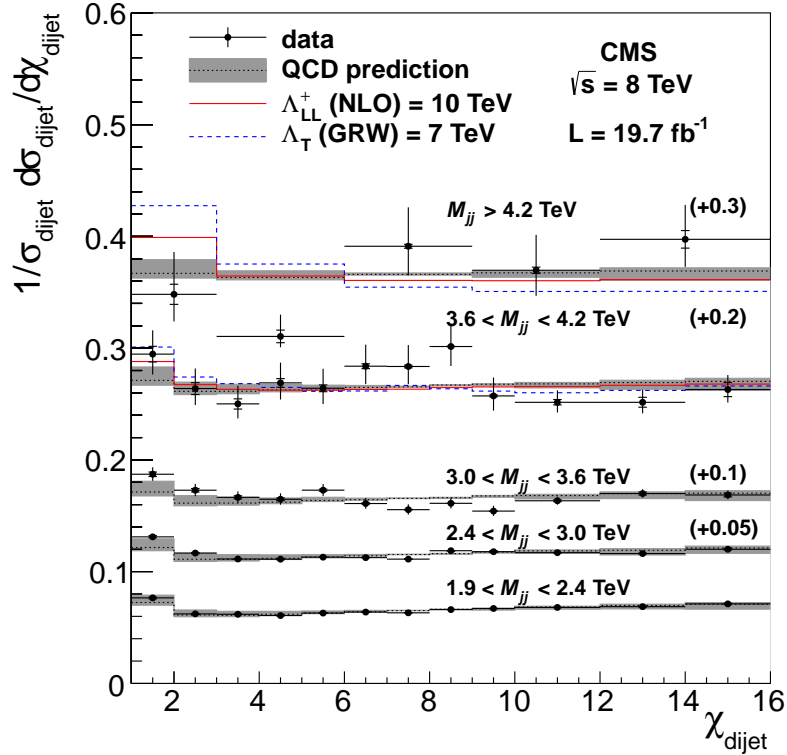


Figure 28: Normalized  $\chi_{dijet}$  distributions for  $19.7 \text{ fb}^{-1}$  of integrated luminosity. The corrected data distributions are compared to NLO predictions with non-perturbative corrections (black dotted line). The individual distributions are shifted vertically by an offset indicated in brackets. Theoretical uncertainties are indicated as a gray band. The error bars represent statistical and experimental systematic uncertainties combined in quadrature. The ticks on the error bars represent experimental systematic uncertainties only. The prediction for QCD+CI with  $\Lambda_{LL}^+$  (NLO) = 10 TeV is shown (red solid line), and so is the prediction for QCD+ADD with  $\Lambda_T$  (GRW) = 8 TeV (blue dashed line).

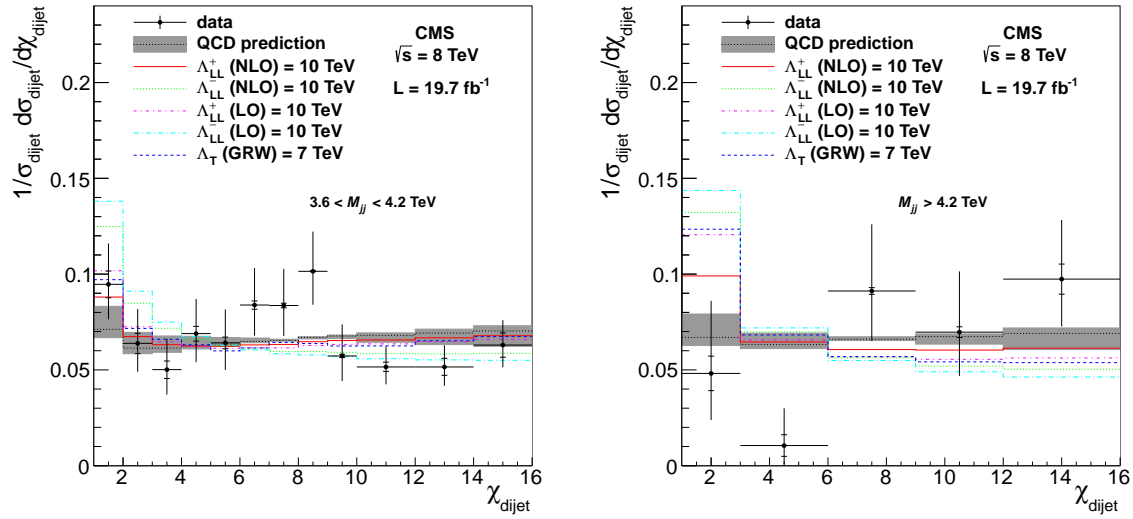


Figure 29: Normalized  $\chi_{dijet}$  distributions for  $19.7 \text{ fb}^{-1}$  of integrated luminosity in the two highest mass bins. The corrected data distributions are compared to NLO predictions with non-perturbative corrections (black dotted line). Theoretical uncertainties are indicated as gray bands. The error bars represent statistical and experimental systematic uncertainties combined in quadrature. The ticks on the error bars represent experimental systematic uncertainties only. The predictions for the various CI and ADD models are overlaid.

Uncertainty	$1.9 < M_{jj} < 2.4 \text{ TeV}$	$M_{jj} > 4.2 \text{ TeV}$
Statistical	0.9%	45%
Jet energy scale	2.0%	3%
Jet energy resolution (core)	0.5%	1.5%
Jet energy resolution (tails)	1.0%	13%
Unfolding, MC modeling	0.1%	1.2%
Unfolding, detector simulation	0.4%	5%
Pileup	<1%	<1%
Total experimental	2.4%	45%
NLO scale (6 variations of $\mu_R$ and $\mu_F$ )	+6.1%	+15%
PDF (CT10 eigenvectors)	-2.1%	-5%
Non-perturbative corrections (Pythia8 vs. Herwig++)	0.6%	1.0%
Total theoretical	<1%	<1%
	6.1%	15%

Table 6: Summary of leading experimental and theoretical uncertainties on the normalized  $\chi_{dijet}$  distributions. While in the statistical analysis each uncertainty is represented by a change of the  $\chi_{dijet}$  distribution correlated among all  $\chi_{dijet}$  bins, this table summarizes each uncertainty by a representative number to demonstrate the relative contributions. For the lowest and highest dijet mass bins, the relative shift (in %) of the lowest  $\chi_{dijet}$  bin from its nominal value is quoted. In the highest dijet mass bin, the dominant experimental contribution is the statistical uncertainty while the dominant theoretical contribution is the scale uncertainty.

## 7 Search for new physics

In this section we explore the sensitivity of this analysis to new physics. In particular, we extract limits on new physics models with a contact interaction (quark compositeness model) or virtual graviton exchange (ADD model) beyond expected QCD interactions. First we describe the method of statistical evaluation. Then the observed and expected limits are presented.

### 7.1 Method of statistical evaluation

We perform a statistical test discriminating between the QCD only hypothesis and the QCD plus New Physics (QCD+NP) hypothesis as a function of the energy scale  $\Lambda$  based on the log-likelihood-ratio

$$Q = \text{test statistics} = -2 \ln \left( \frac{L_{\text{QCD+NP}}}{L_{\text{QCD}}} \right). \quad (6)$$

Here the likelihood functions  $L_{\text{QCD+NP}}$  and  $L_{\text{QCD}}$  are modeled as a product of Poisson likelihood functions for each bin in  $\chi$  and  $M_{jj}$ .

$$L(x_i \text{ for } i \in \text{bins} | \lambda_i \text{ for } i \in \text{bins}) = \prod_{i \in \text{bins}} \frac{\lambda_i^{x_i}}{x_i!} \cdot e^{-\lambda_i} \quad (7)$$

The  $\lambda_i$  correspond to the entries in each bin of the QCD (QCD+NP) model, the  $x_i$  to the entries of the (pseudo-)data. In each  $M_{jj}$  bin the prediction is normalized to the number of data events. For the implementation of the test statistics we use the "combine" package.

The p-values for the two hypotheses  $P_{\text{QCD+NP}}(Q \geq Q_{\text{obs}})$  and  $P_{\text{QCD}}(Q \leq Q_{\text{obs}})$  are obtained using ensembles of pseudo-experiments.  $P_{\text{QCD+NP}}(Q \geq Q_{\text{obs}})$  is the probability to observe a log-likelihood-ratio  $Q$  in the QCD+NP model that is higher than the log-likelihood-ratio  $Q_{\text{obs}}$  observed in (pseudo-)data and  $P_{\text{QCD}}(Q \leq Q_{\text{obs}})$  is the probability to observe a log-likelihood-ratio  $Q$  in the QCD model that is lower than the log-likelihood-ratio  $Q_{\text{obs}}$  observed in (pseudo-)data.

A modified frequentist approach [38, 39] based on the quantity

$$CL_s = \frac{P_{\text{QCD+NP}}(Q \geq Q_{\text{obs}})}{1 - P_{\text{QCD}}(Q \leq Q_{\text{obs}})} \quad (8)$$

is used to set limits on the contact interaction scale. The QCD+NP model is excluded at 95% confidence level if  $CL_s < 0.05$ . This method prevents exclusion that could result from statistical fluctuations in situations where one has no sensitivity but may result in a coverage probability of the corresponding exclusion limits exceeding the nominal confidence level of 95%. For the evaluation of the pseudo-experiments and  $CL_s$  we use HybridNew implementation in the "combine" package.

The uncertainties of the measurement are taken into account as follows. The statistical uncertainties are treated as Poisson distributed around the number of observed data events in each bin in the ensembles of pseudo-experiments. Systematic uncertainties are introduced via Bayesian integration [40] by varying them as nuisance parameters in the ensembles of pseudo-experiments. Note that only shape changing systematic uncertainties which do not change the yield are taken into account since the normalized angular distributions are measured. The systematic uncertainties are modeled using 3 histograms with varied scales of  $-1\sigma$ ,  $0\sigma$ ,  $+1\sigma$  of the expected uncertainty, interpolated using cubic splines with linear extrapolation beyond

$\pm 1\sigma$ . The scale is varied according to a Gaussian prior probability density function, resulting in combination in a Gaussian distribution convoluted with the shape variation induced to the  $\chi_{\text{dijet}}$  distributions. The variation is truncated at 0 events in less than 1% of the cases.

The leading systematic uncertainties, namely the jet energy scale and the  $\mu_F$ ,  $\mu_R$  scales, are taken into account. For the scale uncertainty the maximum variations of the shape of the  $\chi_{\text{dijet}}$  distribution are used to model the uncertainty. The  $+1\sigma$  ( $-1\sigma$ ) histogram is chosen to have the maximal positive (negative) slope. Note that the choice of the Gaussian prior probability density function is ambiguous in this case, as the scale uncertainty is just a rough estimator for higher order perturbative effects and therefore its distribution is unknown. The jet energy scale uncertainty has been derived independently for each scale of  $\Lambda$ , as it differs from the effect observed on the QCD distribution. In this way, the effect of event migration between mass bins is taken into account. As the quark compositeness signal is only prominent in the higher mass bins, event migrations change the prediction in each mass bin, and has to be taken into account.

In the statistical analysis only the two highest mass bins are taken into account, since the lower mass bins were found to have a negligible contribution to the expected exclusion limits on the contact interaction and extra dimension models. Figure 30 summarizes the information entering into the statistical analysis, namely the data distribution, the simulated background and signal distributions, as well the the systematic uncertainties.

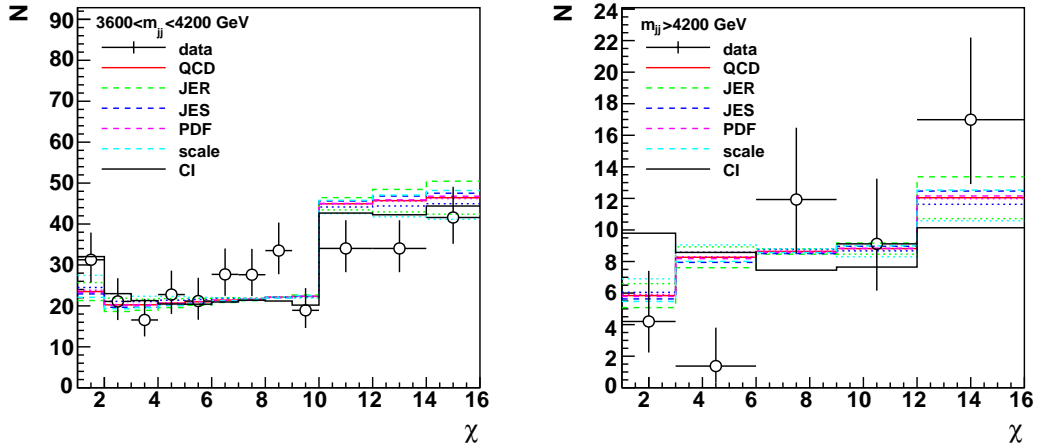


Figure 30: Summary of the input to the statistical analysis.

## 7.2 Significance of the data

We evaluate the significance of the data distributions in four ways. Firstly, we estimate the p-values  $1 - CL_B = P_{\text{QCD}}(Q \leq Q_{\text{obs}})$  for each mass using the contact interaction model in the likelihood ratio which tells how large of an upward fluctuation at low chi as predicted by the contact interaction model is observed. Secondly, we estimate  $P_{\text{QCD}}(Q > Q_{\text{obs}})$  for each mass using an unphysical model with an opposite effect on the chi distribution as the contact interaction model in the likelihood ratio which tells how large of a downward fluctuation at low chi in opposite direction of the contact interaction model is observed. Thirdly, we calculate a simple  $\chi^2/\text{DOF}$ , summing in quadrature systematic and statistical uncertainties and assuming that they are uncorrelated between  $\chi$  bins (which is not true for the systematic uncertainties). Fourth, we perform a goodness of fit test taking into account all uncertainties and their correlations based on the saturated model as described in this note [41] and estimate the significance w.r.t. the expected goodness of fit. The results are summarized in Table 7.

In addition we fit the jet energy resolution nuisance parameter to the data under the QCD-only hypothesis, to quantify by a shift of how many standard deviations of the systematic uncertainty, the data can be explained. The result is in the last column of Table 7. Note that the jet energy resolution is only the dominant uncertainty in the highest mass bin. Therefore, in lower mass bins other systematic uncertainties should be considered as well.

Table 7: Significance of the data distribution.

Mass bins [TeV]	CI-model	Anti-CI-model	$\chi^2/DOF$	GOF	JER shift
4.2	0.1	1.4	1.6	0.4	+1.0
3.6	1.3	0.2	0.9	0.6	-1.2
3.0	1.3	0.1	1.8	1.4	-1.3
2.4	1.1	0.1	1.0	2.0	-2.4
1.9	0.7	0.3	0.7	3.3	-1.3
3.6, 4.2	0.7	0.8	1.2	1.8	-0.5
2.4, 3.0, 3.6, 4.2	1.1	0.1	1.3	-	-2.1
1.9, 2.4, 3.0, 3.6, 4.2	0.8	0.3	1.2	-	-1.8

### 7.3 Limits

Having defined the exclusion criterion  $CL_s < 0.05$  at 95% confidence level, one can exclude parameter ranges for the quark compositeness and extra dimension models. The quark compositeness model is described by an energy scale  $\Lambda$ . As the cross section of the contact interaction in the mass bins of the analysis decreases continuously with increasing  $\Lambda$ , one can set lower limits on the contact interaction scale  $\Lambda$  from the measured dijet angular distributions. The ADD model is described by an energy scale  $\Lambda_T$  or  $M_S$ , which plays a similar role as the contact interaction scale. In the following we talk only about the contact interaction scale  $\Lambda$ , but the same description applies to the ADD scale  $\Lambda_T$  or  $M_S$ .

The limits are obtained by calculating the  $CL_s$  as a function of  $\Lambda$  and finding the crossing point with  $CL_s = 0.05$ . For this calculation, a continuous model of the dijet angular distributions as a function of  $\Lambda$  is needed. It is constructed by interpolating the angular distributions in each mass and  $\chi_{\text{dijet}}$  bin between the contact interaction predictions at the scales 5, 6, 7, 8, 9, 10, 11, 12, 13, 14 and 15 TeV using cubic spline interpolation. The precision of the interpolation has been evaluated to be better than 0.02 TeV in terms of the limit on  $\Lambda$  by comparing to an interpolation with an intermediate prediction removed.

In addition to the limit observed in data, it is important to study also the expected limit given the number of observed data events in each mass bin. The expected limit quantifies the sensitivity of the experiment independent from statistical fluctuations in the data and is therefore important for comparisons with other measurements. The expected  $CL_s$  is evaluated by using the log-likelihood-ratio  $Q_{\langle QCD \rangle}$  at the median of the  $P_{QCD}(Q)$  instead of the  $Q_{\text{obs}}$  of the data. In this way a limit is extracted under the assumption that the data lies at the center of the expectation for the QCD hypothesis.

Additional to the expected limit one can also extract the variation of the expected limit within the uncertainties. By using the log-likelihood ratio  $Q$  at 16% (2.2%) and 84% (97.7%) values of  $P_{QCD}(Q)$ , instead of the median (=50%),  $1\sigma$  ( $2\sigma$ ) bands reflecting the variation of the expected limit, are obtained.

The observed and expected limits at 95% C.L. are listed in Table 8 and summarized in Fig. 31.

Table 8: Observed and expected limits at 95% confidence level for the energy scale for various contact interaction and extra dimension models.

Model	Observed limit	Expected limit
$\Lambda_{LL/RR}^+$ (NLO)	8.8	$8.8 \pm 0.8$
$\Lambda_{LL/RR}^-$ (NLO)	10.9	$11.4 \pm 1.8$
$\Lambda_{LL/RR}^+$ (LO)	9.8	$9.8 \pm 0.9$
$\Lambda_{LL/RR}^-$ (LO)	11.9	$12.5 \pm 2.0$
$\Lambda_{V/A}^+$ (LO)	11.6	$11.7 \pm 1.3$
$\Lambda_{V/A}^-$ (LO)	15.5	$16.3 \pm 2.7$
$\Lambda_{(V-A)}^\pm$ (LO)	8.6	$9.0 \pm 0.8$
ADD $\Lambda_T$ (GRW)	7.0	$7.0 \pm 0.7$
ADD $M_S$ (HLZ) $n_{ED} = 2$	7.2	$7.2 \pm 0.7$
ADD $M_S$ (HLZ) $n_{ED} = 3$	5.9	$5.9 \pm 0.6$
ADD $M_S$ (HLZ) $n_{ED} = 4$	7.0	$7.0 \pm 0.7$
ADD $M_S$ (HLZ) $n_{ED} = 5$	7.7	$7.7 \pm 0.8$
ADD $M_S$ (HLZ) $n_{ED} = 6$	8.3	$8.3 \pm 0.8$

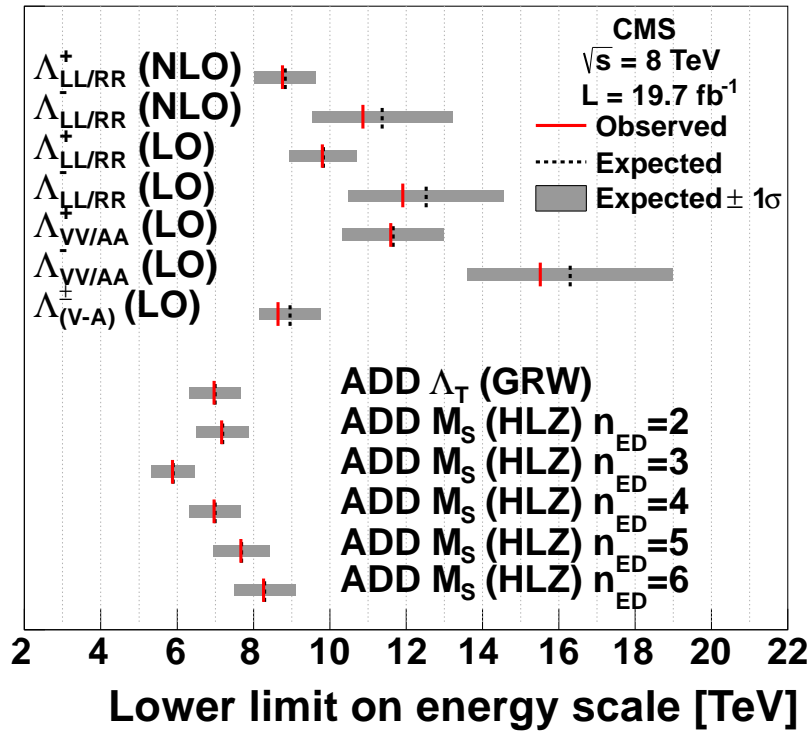


Figure 31: Summary of the limits.

## 8 Summary

The dijet angular distributions in  $M_{jj}$  bins have been measured at CMS using LHC data taken in 2012 at 8 TeV with an integrated luminosity of  $19.7 \text{ fb}^{-1}$ . The  $\chi_{\text{dijet}}$  distributions are compared to theoretical predictions from NLO. The data are found in good agreement with the theory predictions. Limits at the 95 % CL are set on a variety of quark compositeness and large extra dimension signatures.

DRAFT



---

## 427 **9 Appendix**

### 428 **9.1 List of high mass events**

DRAFT

Table 9: High mass events.

Run	LBlock	Event	Mass	Chi
204541	32	52508234	5163.78	1.92379
204576	265	409073019	5140.87	7.44875
194533	325	456947237	5133.19	7.91213
195016	91	109308674	4905.84	10.825
205344	631	702903839	4841.07	12.8694
201196	706	545408136	4832.31	11.8749
202178	403	508731083	4784.84	12.7433
200091	1391	1530956548	4732.32	11.2521
203002	255	337772027	4730.21	4.43648
203912	2	2661553	4709.61	15.0862
194153	66	62170418	4643.48	15.2197
194480	523	475239394	4615.62	12.3129
198955	751	850626328	4587.07	11.7072
198955	1314	1347310134	4580.5	8.3105
199960	298	360409563	4580.45	7.26238
201705	180	229652524	4566.06	15.6609
199608	253	299212426	4560.52	12.7034
203835	205	145704048	4536.36	9.27898
206207	344	515767750	4533.36	12.8653
195915	134	239535563	4519.3	13.889
206187	143	140588083	4503.46	12.6158
205515	170	196499575	4484.73	10.2742
199833	196	242450225	4473.56	12.2591
207222	202	187158596	4457.68	9.57453
207905	940	1234286744	4436.89	13.52
200600	691	890725542	4409.51	7.7009
199319	12	18709167	4383.01	7.96089
200381	20	35563318	4355.78	15.7074
196334	295	455111506	4341.82	9.76617
195656	137	125717172	4336.16	10.6791
206210	48	46950785	4330.0	5.20723
194050	1113	1039802089	4326.06	15.3041
202060	174	185478950	4319.91	9.08708
205921	570	805221508	4314.57	3.66015
207922	79	89405853	4307.09	7.36654
199812	200	221479047	4307.05	12.4296
206088	214	287106172	4296.69	11.088
195649	185	271127396	4292.89	1.80887
200091	1678	1762558729	4266.42	10.3389
202045	56	68940337	4263.95	12.3611
206596	801	857310180	4258.7	13.5718
206207	114	115656329	4257.63	1.93396
199021	542	655562492	4256.12	9.46438
206389	135	126604242	4252.16	11.8885
196199	318	368109579	4240.03	13.2768
200473	569	611965930	4238.23	11.2357
206859	651	956958815	4225.38	2.12589
205826	90	69966952	4219.72	14.6343
206598	619	492086444	4209.67	7.58854
201802	76	33273619	4201.33	2.36233

## References

- [1] "D0 Collaboration", "Measurement of Dijet Angular Distributions at  $\sqrt{s} = 1.96 \text{ TeV}$  and Searches for Quark Compositeness and Extra Spatial Dimensions", *Phys. Rev. Lett.* **103** (2009) 191803. doi:10.1103/PhysRevLett.103.191803.
- [2] "D0 Collaboration", "High- $p_T$  jets in  $p\bar{p}$  collisions at  $\sqrt{s} = 630$  and  $1800 \text{ GeV}$ ", *Phys. Rev. D* **64** (2001) 032003. doi:10.1103/PhysRevD.64.032003.
- [3] CDF Collaboration, "Measurement of Dijet Angular Distributions at CDF", [Erratum-ibid. **78**, 4307 (1997)] *Phys. Rev. Lett.* **77** (1996) 5336. doi:10.1103/PhysRevLett.77.5336.
- [4] ATLAS Collaboration, "ATLAS Search for New Phenomena in Dijet Mass and Angular Distributions using pp Collisions at  $\sqrt{s} = 7 \text{ TeV}$ ", *JHEP* **1301** (2013) 029. doi:10.1007/JHEP01(2013)029.
- [5] ATLAS Collaboration, "Search for New Physics in Dijet Mass and Angular Distributions in pp Collisions at  $\sqrt{s} = 7 \text{ TeV}$  Measured with the ATLAS Detector", *New J. Phys.* **13** (2011) 053044. doi:10.1088/1367-2630/13/5/05044.
- [6] ATLAS Collaboration, "Search for Quark Contact Interactions in Dijet Angular Distributions in pp Collisions at  $\sqrt{s} = 7 \text{ TeV}$  Measured with the ATLAS Detector", *Phys. Lett. B* **694** (2010) 327. doi:10.1016/j.physletb.2010.10.021.
- [7] CMS Collaboration, "Search for Quark Compositeness in Dijet Angular Distributions from pp Collisions at  $\sqrt{s} = 7 \text{ TeV}$ ", *JHEP* **05** (2012) 055. doi:10.1007/JHEP05(2012)055.
- [8] CMS Collaboration, "Measurement of Dijet Angular Distributions and Search for Quark Compositeness in pp Collisions at  $\sqrt{s} = 7 \text{ TeV}$ ", *Phys. Rev. Lett.* **106** (2011) 201804. doi:10.1103/PhysRevLett.106.201804.
- [9] CMS Collaboration, "Search for Quark Compositeness with the Dijet Centrality Ratio in pp Collisions at  $\sqrt{s}=7 \text{ TeV}$ ", *Phys. Rev. Lett.* **105** (2010) 262001. doi:10.1103/PhysRevLett.105.262001.
- [10] E. Eichten, K. Lane, and M. Peskin, "New tests for quark and lepton substructure", *Phys. Rev. Lett.* **50** (1983) 811. doi:10.1103/PhysRevLett.50.811.
- [11] E. Eichten et al., "Supercollider Physics", *Rev. Mod. Phys.* **56** (1984) 579. doi:10.1103/RevModPhys.56.579.
- [12] K. Nakamura et al. (Particle Data Group), "Review of Particle Physics", *J. Phys. G: Nucl. Part. Phys.* **37** (2010) 075021. doi:10.1088/0954-3899/37/7A/075021.
- [13] CMS Collaboration, "Search for contact interactions using the inclusive jet  $p_T$  spectrum in pp collisions at  $\sqrt{s} = 7 \text{ TeV}$ ", *Phys. Rev. D* **87** (2013) 052017. doi:10.1103/PhysRevD.87.052017.
- [14] N. Arkani-Hamed, S. Dimopoulos, and G. Dvali, "The hierarchy problem and new dimensions at a millimeter", *Phys. Lett. B* **429** (1998) 263. doi:10.1016/S0370-2693(98)00466-3.

- [15] N. Arkani-Hamed, S. Dimopoulos, and G. Dvali, "Phenomenology, astrophysics and cosmology of theories with sub-millimeter dimensions and TeV scale quantum gravity", *Phys. Rev. D* **59** (1999) 086004. doi:10.1103/PhysRevD.59.086004.
- [16] G. Giudice, R. Rattazzi, and J. Wells, "Quantum gravity and extra dimensions at High-Energy Colliders", *Nucl. Phys. B* **544** (1999) 3. doi:10.1016/S0550-3213(99)00044-9.
- [17] T. Han, J. Lykken, and R. Zhang, "On Kaluza-Klein States from Large Extra Dimensions", *Phys. Rev. D* **59** (1999) 105006. doi:10.1103/PhysRevD.59.105006.
- [18] CMS Collaboration, "Search for large extra dimensions in dimuon and dielectron events in pp collisions at  $\sqrt{s} = 7$  TeV", *Phys. Lett. B* **711** (2012) 15. doi:10.1016/j.physletb.2012.03.029.
- [19] ATLAS Collaboration, "Search for contact interactions and large extra dimensions in dilepton events from pp collisions at  $\sqrt{s} = 7$  TeV with the ATLAS detector", *Phys. Rev. D* **87** (2013) 015010. doi:10.1103/PhysRevD.87.015010.
- [20] CMS Collaboration, "Search for signatures of extra dimensions in the diphoton mass spectrum at the Large Hadron Collider", *Phys. Rev. Lett.* **108** (2012) 111801. doi:10.1103/PhysRevLett.108.111801.
- [21] ATLAS Collaboration, "Search for Extra Dimensions in diphoton events using proton-proton collisions recorded at  $\sqrt{s} = 7$  TeV with the ATLAS detector at the LHC", *New J. Phys.* **15** (2013) 043007. doi:10.1088/1367-2630/15/4/043007.
- [22] D0 Collaboration, "Measurement of dijet angular distributions at  $\sqrt{s} = 1.96$  TeV and searches for quark compositeness and extra spatial dimensions", *Phys. Rev. Lett.* **103** (2009) 191803. doi:10.1103/PhysRevLett.103.191803.
- [23] R. Franceschini, G. Giudice, P. Giardino et al., "LHC bounds on large extra dimensions", *JHEP* **05** (2011) 092. doi:10.1007/JHEP05(2011)092.
- [24] CMS Collaboration, "The CMS experiment at the CERN LHC", *JINST* **3** (2008) S08004. doi:10.1088/1748-0221/3/08/S08004.
- [25] CMS Collaboration, "Jet in 0.9 and 2.36 TeV pp Collisions", *CMS Physics Analysis Summary* **CMS-PAS-JME-10-001** (2010).
- [26] CMS Collaboration, "Determination of Jet Energy Calibration and Transverse Momentum Resolution in CMS", *JINST* **06** (2011) 11002. doi:10.1088/1748-0221/6/11/P11002.
- [27] T. Sjostrand, S. Mrenna, and P. Skands, "PYTHIA 6.4 Physics and Manual", *JHEP* **05** (2006) 026. doi:10.1088/1126-6708/2006/05/026.
- [28] GEANT4 Collaboration, "G4—a simulation toolkit", *NIM* **A506** (2003).
- [29] CMS Collaboration, "Jet Energy Resolutions Derived from QCD Simulation for the Analysis of First  $\sqrt{s} = 7$  TeV Collision Data", CMS AN-2010/121.
- [30] CMS Collaboration, "Jet position resolutions in 7 TeV data", CMS AN-2010/121.

- [31] G. D'Agostini, "A multidimensional unfolding method based on Bayes' theorem", *Nuclear Instruments and Methods in Physics Research Section A: Accelerators, Spectrometers, Detectors and Associated Equipment* **362** (1995), no. 23, 487 – 498.  
doi:[http://dx.doi.org/10.1016/0168-9002\(95\)00274-X](http://dx.doi.org/10.1016/0168-9002(95)00274-X).
- [32] T. Adye, "Unfolding algorithms and tests using RooUnfold", in *Proceedings of the PHYSTAT 2011 Workshop on Statistical Issues Related to Discovery Claims in Search Experiments and Unfolding*, pp. 313–318. Geneva, Switzerland, January, 2011.  
arXiv:1105.1160.
- [33] Z. Nagy, "Three-jet cross sections in hadron hadron collisions at next-to-leading order", *Phys. Rev. Lett.* **88** (2002) 122003. doi:10.1103/PhysRevLett.88.122003.
- [34] T. Kluge, K. Rabbertz, and M. Wobisch, "Fast pQCD calculations for PDF fits", in *14th International Workshop on Deep Inelastic Scattering (DIS 2006), 20-24 Apr 2006*, pp. 483–486. Tsukuba, Japan, April, 2006. arXiv:hep-ph/0609285.
- [35] M. Heinrich, A. Oehler, K. Rabbertz, "NLO Calculations for Inclusive Jets with fastNLO at 10 TeV", *AN-2009-058* (2009).
- [36] P. M. Nadolsky et al., "Implications of CTEQ global analysis for collider observables", *Phys. Rev. D* **78** (2008) 013004. doi:10.1103/PhysRevD.78.013004.
- [37] J. Gao et al., "Next-to-leading QCD effect to the quark compositeness search at the LHC", *Phys. Rev. Lett.* **106** (2011) 142001. doi:10.1103/PhysRevLett.105.262001.
- [38] T. Junk, "Confidence Level Computation for Combining Searches with Small Statistics", *Nucl. Instrum. Meth. A* **434** (1999) 435. doi:10.1016/S0168-9002(99)00498-2.
- [39] A. L. Read, "Modified frequentist analysis of search results", in *First Workshop on Confidence Limits*, pp. 81–101. CERN. Geneva, Switzerland, 2000.
- [40] R. D. Cousins and V. L. Highland, "Incorporating systematic uncertainties into an upper limit", *Nucl. Instrum. Meth. A* **320** (1992) 331.  
doi:10.1016/0168-9002(92)90794-5.
- [41] "Saturated model for goodness of fit",  
[http://www.physics.ucla.edu/~cousins/stats/cousins\\_saturated.pdf](http://www.physics.ucla.edu/~cousins/stats/cousins_saturated.pdf).